Quantile-based robust optimization of a supersonic nozzle for organic rankine cycle turbines

Nassim Razaaly, Giacomo Persico, Giulio Gori, Pietro Marco Congedo

Quantile-based robust optimization of a supersonic nozzle for Organic Rankine Cycle turbines

Nassim RAZAALY[a], Giacomo PERSICO[b], Giulio GORI[a], Pietro Marco CONGEDO[a,*]

[a]*DeFI Team (INRIA Saclay IDF, Ecole Polytechnique), CMAP Laboratory, 1 rue d'Estienne d'Orves 91120 Palaiseau, France.*
[b]*Laboratorio di Fluidodinamica delle Macchine, Politecnico di Milano, Via Lambruschini 4, I-20156 Milano, Italy.*

Abstract

Organic Rankine Cycle (ORC) turbines usually operate in thermodynamic regions characterized by high-pressure ratios and strong non-ideal gas effects, complicating the aerodynamic design significantly. Systematic optimization methods accounting for multiple uncertainties due to variable operating conditions, referred to as Robust Optimization may benefit to ORC turbines aerodynamic design. This study presents an original and fast robust shape optimization approach to overcome the limitation of a deterministic optimization that neglects operating conditions variability, applied to a well-known supersonic turbine nozzle for ORC applications. The flow around the blade is assumed inviscid and adiabatic and it is reconstructed using the open-source SU2 code. The non-ideal gasdynamics is modeled through the Peng-Robinson-Stryjek-Vera equation of state. We propose here a mono-objective formulation which consists in minimizing the α-quantile of the targeted Quantity of Interest (QoI) under a probabilistic constraint, at a low computational cost. This problem is solved by using an efficient robust optimization approach, coupling a state-of-the-art quantile estimation and a classical Bayesian optimization method. First, the advantages of a quantile-based formulation are illustrated with respect to a conventional mean-based robust optimization. Secondly, we demonstrate the effectiveness of applying this robust optimization framework with a low-fidelity inviscid solver by comparing the resulting optimal design with the ones obtained with a deterministic optimization using a fully turbulent solver.

Keywords: Robust Optimization, Blade Shape Optimization, Quantile, Surrogate-Based Optimization, Gaussian-Processes, Uncertainty Quantification

1. Introduction

Organic Rankine Cycle (ORC) power systems, based on the application of organic compounds as working fluids in heat exchangers and turbomachinery, has seen a dramatic technical and economic growth in the last decade. The variety guaranteed by the broad spectrum of available organic fluids matches the diverse requirements of widely distributed thermal energy conversion devices [1, 2], which feature a multiplicity of heat sources (solar thermal collectors, geothermal applications, waste heat from industrial processes, etc). Such sources typically feature variable loads and, hence, the thermodynamic conditions at the exit of the boiler/inlet of the turbine undergo large variations; variations combine with the natural seasonal change in ambient temperature, which might alter the thermodynamic conditions of the condenser/outlet of the turbine. These variations result in considerable differences in the turbine operation and, in particular, in a variable aerodynamic load on the cascades of the machine, potentially reducing the

*Corresponding author. Tel.: +33(0)172925935
E-mail address: pietro.congedo@inria.fr

turbine performance with respect to the design condition. This behavior is particularly significant in the present context since, due to the peculiar thermodynamic behavior of organic fluids, ORC turbines feature few stages with high expansion ratio and, hence, operate in supersonic/transonic conditions. As well known, supersonic turbines are prone to the onset of shocks, which grow significantly in strength (and in related aerodynamic loss) as soon as the turbine exits from design conditions. Therefore, the designer should take into account the robustness to variation in operating conditions to improve the reliability of ORC technology.

In present-day turbomachinery design, fluid-dynamic shape optimization (FSO) methods are routinely applied and have recently undergone a significant improvement, offering the possibility to deal with complex problems at a reduced computational cost [3]. Those methodologies play an even more important role in the case of technologies entailing the non-ideal compressible fluid dynamics (NICFD), such as ORC turbines, for which design experience and experimental information are limited to very few cases (see [4] for the very first experiments on NICFD in supersonic nozzles). In the last five years, concerted research efforts have been devoted to develop FSO techniques for NICFD applications, such as for nozzles and turbomachinery blades, using either gradient-based ([5] [6] [7]) or gradient-free algorithms ([8] [9] [10]); a more systematic comparison between these two classes of optimization, when applied to ORC turbines, is reported in [11]. In such studies, deterministic formulations of the optimization problem have always been considered, despite the variability mentioned above in operating conditions. A multi-point approach based on stochastic concepts is also proposed in [12] to account for operational variability.

The present paper aims at providing a novel contribution to the design of turbomachinery by proposing an original shape optimization approach. The method overcomes the limitations of deterministic optimizations in the presence of operative variability by modeling this latter as a random vector, and introducing the quantification of the related uncertainty within what is called *robust* optimization process. In general, we can define robustness as the ability to guarantee a performance which is less sensitive to uncertainties. Classically, the Taguchi paradigm is applied to ensure robustness [13] *i.e.*, the maximization of the mean performance while minimizing the associated variance. The present paper proposes a novel method that, differently than other approaches proposed in Literature, focuses on the quantile.

Robust optimization techniques featuring the explicit uncertainty quantification suffer from dimensionality issues, due to a large number of fluid-dynamic calculations required, which eventually determine the technical feasibility of the method. Surrogate-based techniques are primarily used to limit the overall computational cost; see for example [14] or [15], where a kriging-based Sequential Approximate Optimization (SAO) strategy is illustrated. A discussion over the interest in using surrogate models for uncertainty-based optimization is presented in [16], where Kriging and more generally Gaussian Process (GP) techniques are shown to be very promising. In this context, [17] proposes a formulation based on a target performance and variance minimization of a specific Quantity of Interest (QoI); the performance function is approximated with a kriging model in coupled space, and low-cost Monte Carlo sampling on the model allows to build a second kriging metamodel on the statistical moments. In [18], a GP model is used to perform mean performance optimization, and optimization is achieved through Bayesian Optimization (BO). Regarding the minimization algorithm, GP-based techniques such as the Efficient Global Optimization (EGO) have been massively used in optimization (see for example [19] or [20].

Even though nowadays established and fully demonstrated, RO aimed at minimizing the mean of a QoI might suffer from a lack of control of this latter variability. This aspect is particularly relevant for ORC turbines since the variability is concerning operating conditions and the flow configuration is supersonic, so the performance sensitivity to input uncertainty might be significant. Alternative formulations are possible to enhance the control of the variability, taking into account the QoI's standard deviation, for example by formulating the objective function as $\mu \pm k\sigma$, or Min σ s.t. $\mu < \mu_0$ for instance, where μ, σ denote the QoI's mean and standard deviation respectively. However, such methods suffer from the fact that the user-defined parameters k, μ_0 have a substantial impact on the final design. Moreover, including explicitly the standard deviation in the objective function significantly increases the computation burden. In ORC applications, multi-objective optimization have been proposed considering both the mean and the standard deviation [21–23]; as already recalled, a multi-point approach was also proposed [12].

In this paper, we propose to minimize a high quantile of the QoI in the context of the ORC turbine blade optimization. It has the advantage of being highly interpretable: the QoI's 95% quantile is the threshold below which 95% of the QoI's realizations lie, involving that designer may choose a specific quantile level according to some technical constraints. The quantile can be easily evaluated as a function of the standard deviation σ, once the probability density functions (PDF) is assigned (for example, 2σ represents q_{95} for a gaussian QoI). However, in robust optimization

problems applied to aerodynamic design, which feature large uncertainties and severe non-linear effects, the PDF of the QoI is not known apriori. As a second consideration, evaluating the quantile with classical Monte-Carlo methods is not cost-effective with respect to σ evaluation; however, state-of-the-art surrogate-based techniques permits the leverage this issue, by using a learning technique which exploits the local nature of the quantile, whose assessment can be seen as an inverse problem for tail probability computation. As shown in this article, the cost to evaluate the quantile can be even lower, or in any case of the same order of magnitude as the cost of assessing the average for example. The use of quantile can, however, be particularly beneficial in controlling the PDF of the optimal design, compared to optimizing an integral quantity such as the mean or the standard deviation.

By virtue of such considerations, the proposed method relies on a double-loop algorithm coupling an efficient quantile estimation [24], and a bayesian optimization technique [25]. The proposed approach is applied here to the constrained robust optimization of a well-known supersonic turbine nozzle for ORC applications [26], that was considered for deterministic optimization with both inviscid [5] and Reynolds-Averaged Navier-Stokes (RANS) [6, 9] models. It requires an automated sequence of operations consisting of the parameterization of the blade, mesh generation and finally the CFD evaluation to compute the QoI. A mesh-convergence study is presented to assess the CFD solution and the influence of the numerical error within the optimization process. We systematically use an inviscid flow solver for the robust optimizations; in addition, we also present deterministic optimizations perfomed using both inviscid and RANS-based flow model, for comparison. In this way, the impact of usign an inviscid model in spite of the RANS one can be properly evaluated, at least at deterministic level; moreover, the RANS-based optimization can be directly compared with similar high-fidelity optimization efforts recently documented in Literature ([6, 9]), thus validating the optimization chain used in this paper. All the optimal configurations are subsequently analyzed and compared by computing their QoI statistics with the RANS solver. In this article, we show therefore that for the ORC application, which feature large varability in the actual operation, the use of a robust optimization method produces more efficient designs (in stochastic sense) with respect to those that could be obtained using a classical deterministic optimization, independently from the fact that this latter is performed with invisicd or RANS flow models. This study, therefore, proposes a concrete alternative to the optimization of ORC turbines with a systematic consideration of the uncertainties of the system.

The paper is organized as follows. The problem of interest and a sketch of the numerical framework is illustrated in Section 2. Section 3 is devoted to the description of the CFD simulations, design parameterization and numerical verification. In Section 4, the stochastic and optimization algorithms are described in details. In Section 5, the optimization results are discussed, and the evidence about the interest of the proposed framework is provided. Conclusions and some perspectives are then provided in Section 6.

2. Problem Formulation and numerical framework

A classical single-objective optimization problem with constraints can be formulated as follows

$$\begin{aligned} &\text{Minimize} && f(\mathbf{x}) \\ &\text{s.t.} && g(\mathbf{x}) \in [g_{min}, g_{max}] \\ & && \mathbf{x} \in \Omega \end{aligned} \tag{1}$$

where f is a scalar QoI depending on a design vector $\mathbf{x}$ belonging to the design space Ω, and g is a constraint, which can assume values in the interval $[g_{min}, g_{max}]$.

If the problem is affected by uncertainties, then functions f and g depend also on a vector of random variables, denoted as $\boldsymbol{\xi}$. In this case, a very common way of extending the problem mentioned in 1, is to consider some meaningful statistics of the function f and g. For example, the *mean-based optimization* problem consists in:

$$\begin{aligned} &\text{Minimize} && \mathbb{E}_{\boldsymbol{\xi}}[f(\mathbf{x}, \boldsymbol{\xi})] \\ &\text{s.t.} && \mathbb{E}_{\boldsymbol{\xi}}[g(\mathbf{x}, \boldsymbol{\xi})] \in [g_{min}, g_{max}] \\ & && \mathbf{x} \in \Omega \end{aligned} \tag{2}$$

where $\mathbb{E}_{\boldsymbol{\xi}}[\cdot]$ represents the expectation operator conditioned over the random vector $\boldsymbol{\xi}$.

The idea of optimizing a combination of statistics stems from the need of limiting the variability of the QoI; alternatively from the aforementioned approach based on the mean objective function, we propose to solve the following *quantile-based optimization* problem:

$$\begin{aligned} \text{Minimize} \quad & q_{95}^{\boldsymbol{\xi}}[f(\mathbf{x},\boldsymbol{\xi})] \\ \text{s.t.} \quad & \mathbb{E}_{\boldsymbol{\xi}}[g(\mathbf{x},\boldsymbol{\xi})] \in [g_{min}, g_{max}] \\ & \mathbf{x} \in \Omega \end{aligned} \tag{3}$$

where $q_{95}^{\boldsymbol{\xi}}[f(\mathbf{x},\boldsymbol{\xi})]$ represents 95% quantile of f under the probability measure of the random vector $\boldsymbol{\xi}$, satisfying a probabilistic constraint on g.

In this study, we illustrate the interest of such formulation of robust optimization comparing mean-based and quantile-based optimizations in terms of computational cost and robustness of optimal individuals.

We denote here with f and g the outcomes of the CFD-based simulation, which relies on several steps, described in Section 3, including a verification analysis about the mesh convergence.

All the optimizations and UQ analyses reported in this paper are performed using Gaussian Process (GP) surrogates. Surrogates are systematically built over the space of design parameters $\mathbf{x}$, making use of different functions according to the metrics used for the optimization problem: deterministic optimization (f), quantile-based robust optimization (q_{95}), and also a mean-based robust optimization (μ), which is used as a benchmark for the novel quantile-based optimization here proposed. Note also that a GP surrogate of the constraint function g over the space of design parameters $\mathbf{x}$ is built. The GP surrogate construction is illustrated in Section 4.1. An Expected Improvement (EI)-based strategy is then applied for solving the optimization problem, which is presented in Section 4.3.

3. CFD-based simulation

The QoIs *i.e.*, f and g, are computed by means of CFD simulations carried out for given vectors of design parameter $\mathbf{x}$ and uncertainties $\boldsymbol{\xi}$. This evaluation requires the fulfillment of several steps, which are depicted in Figure 1. Subsections 3.1, 3.2, 3.3, and 3.4 describe respectively the flow solver, the turbine cascade configuration and the related nominal and random operating conditions, the mesh generation, and the parametrization of the blade profile. Finally, Subsection 3.5 illustrates the quantities used for assessing the performances of the turbine cascade.

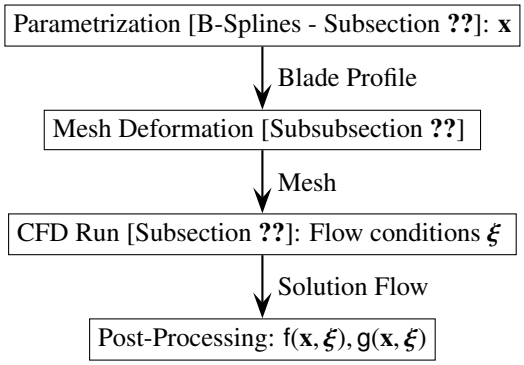

Figure 1: CFD-based evaluation: $f(\mathbf{x},\boldsymbol{\xi})$

3.1. CFD model

The Non-Ideal Compressible-Fluid Dynamics (NICFD) solver included in the SU2 [27–29] suite is employed to carry out the numerical analysis. The reliability of solver predictions against experiments was assessed in [30]. The

SU2 NICFD solver relies on an embedded thermodynamic library which includes several Equations of State (EoS) such as the van der Waals and the Peng-Robinson (PR) ones.

In the following, a brief overview of the main features of a non-ideal solver are highlighted.

The three-dimensional Navier-Stokes equations for compressible flows read

$$\frac{\partial \mathbf{u}}{\partial t} + \nabla \cdot \mathbf{f}(\mathbf{u}) = \nabla \cdot \mathbf{d}(\mathbf{u}) \tag{4}$$

The vector of the conserved variables $\mathbf{u} = (\rho, \mathbf{m}, E^t)^T$ includes the mass density $\rho \in \mathbb{R}^+$, the three components of momentum density $\mathbf{m} \in \mathbb{R}^3$, and the total specific energy $E^t \in \mathbb{R}^+$, $E^t = \rho\left(e + \frac{1}{2}\|\mathbf{v}\|^2\right)$ (where e is the specific internal energy while $\mathbf{v} = \mathbf{m}/\rho$ is the velocity vector).

The functions $\mathbf{f}(\mathbf{u}) = [\mathbf{m}, (\mathbf{m}\otimes\mathbf{m})/\rho + P\mathbf{I}, \mathbf{m}(E^t + P)/\rho]^T$ and $\mathbf{d}(\mathbf{u}) = [\mathbf{0}, \mathbf{\Pi}, \mathbf{v}^T \cdot \mathbf{\Pi} - \mathbf{q})]^T \in \mathbb{R}^5 \times \mathbb{R}^3$ are, respectively, the advection and pressure fluxes, and the the viscous and thermal fluxes. In these latter functions, $P = P(\mathbf{u})$ is the pressure, $\mathbf{I}$ is the identity matrix of dimension 3, $\mathbf{\Pi} = \mathbf{\Pi}(\mathbf{v})$ is the viscous stress tensor and $\mathbf{q}$ is the thermal flux.

The system of equations is supplemented by constitutive relations that bound the state of the fluid to the thermodynamic and to the transport quantities. For a single-component fluid in single-phase conditions, EoS are needed to provide the functional dependency of a state variable from any given pair of independent thermodynamic variables, for instance in the form of $P = P(T, v)$ and $e = e(T, v)$. These relations are invertible and therefore the functional forms $T = T(P, v)$ or $v = v(T, e)$ also exist. The structure of the numerical solver is of course strictly related to these functional relations. From a numerical perspective, when the Ideal Gas EoS is employed a set of simplifications are possible. When more complex EoS are considered, a generalized approach is needed. Therefore, to extend a solver to Non-Ideal flows one has to heavily modify the structure of the code. The efforts made to extend the SU2 solver to NICFD are described in [31].

In the analysis presented hereinafter, the inviscid fluxes are discretized using a MUSCL approach based on an approximate Riemann solver (ARS) of Roe upwind type [32–34] along with the slope limiter proposed by van Albada.

To retrieve the effects of turbulence in RANS simulations, the Menter's k-ω Shear Stress Transport (SST) [35] model is used because of its capability of resolving the near-wall region of the boundary layer as well as the free-stream region, making it widespread in turbomachinery applications.

The SU2 suite is also equipped with Non-Reflecting Boundary Conditions (NRBC) [36] which are exploited throughout this work. NRBC are designed to avoid spurious pressure oscillations due to the reflection of spurious pressure waves at domain boundaries.

3.2. Turbine configuration

The turbine configuration of interest is a well known axial-flow supersonic nozzle cascade operating with siloxane MDM, first presented in [26]. The properties of the MDM are reported in Table 1; in all the calculations the thermodynamic behaviour of the fluid is described by the Peng-Robinson-Stryjek-Vera Equation of State. Uniform thermo-physical quantities are also assigned, estimated as representative values for the entire transformation by resorting to the RefProp library.

Critical pressure	14.152 bar
Critical temperature	564.1 K
Critical density	256.82 $kg.m^{-3}$
γ	1.0165
Acentric factor ω	0.529
Gas constant	35.152 J/kg/K
μ	1.1517×10^{-5} Pa.s
k	0.03799 W/(m.K)

Table 1: Gas properties of the siloxane MDM

Since this work aims at the aerodynamic optimization of the blade profile, the flow model focuses on the two-dimensional flow around the blade profiles at the midspan section of the cascade. Total Pressure P^t_{in}, total Temperature

T^t_{in}, and axial flow direction are assigned at the inlet, while static pressure P^s_{out} is given at the outlet. The inlet turbulent parameters are assigned considering the a typical turbomachinery environment, namely a turbulence intensity of 3% and a turbulent-to-molecular viscosity ratio of 100.

The cascade operates with a design expansion ratio of about 7.5, expanding the organic fluid from 8 bar and 545 K as reported in Table 2. As already recalled in the Introduction, ORC power systems operate in a context of continuous variability that alter the thermodynamic conditions both at the inlet and at the outlet of the turbine. Such variability propagates within the turbine and results in a change of boundary conditions for each cascade. Following [12], in this study we model the operational variability as independent and uniform uncertainties on all the thermodynamic conditions, resulting in the random vector $\boldsymbol{\xi} = [P^t_{in}, T^t_{in}, P^s_{out}]$. The range of these uncertainties is also reported in Table 2. Note that the selection of the test-cases and the prescribed ranges of variability are based on previous experiences of the authors and on the very few information on the topic available from literature. However, the aim of the paper is not to optimize a specific technical case but to investigate a challenging optimization problem for that robust design has an evident technical relevance.

	P^t_{in}	T^t_{in}	P^s_{out}
Nominal	8 bars	545.15 K	1.072 bars
Random	$\mathcal{U}[7.6, 8.4]$ bars	$\mathcal{U}[541.15, 549.15]$ K	$\mathcal{U}[1, 2]$ bars

Table 2: Operating Conditions: Nominal and Random (Uniform and independent).

Note that we neglect the uncertainties on the parameters of the TD model since previous studies [21] provided evidence about their limited impact with respect to the uncertainties on operating conditions for turbine cascades.

A potential interest could be to include the epistemic uncertainty associated with a specific choice of the thermodynamic model. However, given the increase in the calculation cost that would be associated, it would be preferable to use a more accurate equation of state, which however is not available within the SU2 suite. If we add this effect, we should modify this strategy by inserting a multi-fidelity representation of the CFD result. In this work, by relying on all the results presented in the literature [21, 22], we assume that the results of the optimization would hardly be different since the estimated effect of the TD model is systematically negligible compared to other sources of uncertainty.

3.3. Mesh Generation/Deformation

The calculations presented in this paper required the development and application of dedicated mesh generation and mesh deformation tools, as during the optimization process several blade profiles are progressively generated and the mesh has to be modified at each design step. The mesh generation is described in Subsubsection 3.3.1, while the Subsubsection 3.3.2 explains how the initial mesh is deformed during optimization.

3.3.1. Mesh Generation

The numerical grids are generated using an in-house tool based on an advancing-front/Delaunay algorithm. To create hybrid grids suitable for viscous simulations, quadrilateral elements are first added over the solid walls, to build a boundary layer mesh. Afterwards, the advancing front algorithm triangulates the remaining portion of the computational domain. The typical fish-tail shock pattern occurs [26] at the blade trailing edge. Thherefore, grids are properly refined in the regions where shock waves are expected to develop.

In this study, both the Euler and the RANS models are considered to model the flow developing around the blade Grids addressed to inviscid (Euler model-based) simulations require a special treatment of the blade trailing edge region. In the Euler model, the lack of viscosity prevents the inviscid flow to detach from solid boundaries and this may lead to non-physical solutions, especially when the wall is subject to a smooth but strong curvature. The inherent numerical viscosity arising from the discretization of the Euler equations somehow allows to retrieve the separation that does occur at the trailing edge of a blade. However, as the artificial viscosity depends on the local cell size, the separation point also depends on the mesh resolution; with the typical refinement levels employed for transonic/transonic flows in turbine cascades, the separation point might be ill-predicted, leading to local non-physical

states and convergence issues. The truncation of the geometry at the trailing edge introduces two sharp corners that enforce the separation of the flow, generally yielding to an improved convergence rate. For this reason a truncated trailing edge is employed for all the inviscid simulations. Conversely, the original round trailing edge is retained for RANS simulations.

In Navier-Stokes simulations, the height of the first cell of the boundary layer grid is set to $2 \cdot 10^{-7}$ [m], which corresponds to $y^+ \approx 1$. The y^+ value is evaluated starting from flat plate correlations considering the fluid viscosity provided in Table 1, the stream velocity and the density resulting from Euler simulations at the cascade-exit, and blade chord as reference length.

3.3.2. Mesh Deformation

In this study, we employ a grid deformation strategy in order to accommodate the boundary displacement due to the optimization process. The present approach follows the work of [37], successfully applied in [5], to achieve a highly flexible and robust deformation tool for unstructured meshes, based on the interpolation of boundary nodes displacements to the whole mesh with Radial Basis Function (RBF's). A linear system of equations only involving boundary nodes has to be solved, and no grid connectivity information is needed.

Notations. The following notations will be adopted in this subsubsection only. d denotes the dimension space (here $d = 2$), $\mathbf{x} \in \mathbb{R}^d$ a node in the mesh, $\mathbf{x}_{new} \in \mathbb{R}^d$ its new location, n_b the number of boundary nodes, $\{\mathbf{x}_{b_j}\}_{j \in [\![1, n_b]\!]}$ the set of nodes at the boundary, p a polynomial.

The interpolation function $s : \mathbb{R}^d \to \mathbb{R}^d$, describing the displacement in the whole domain, can be written as a sum of basis functions:

$$s(\mathbf{x}) = \sum_{j=1}^{n_b} \alpha_j \Phi(\left\|\mathbf{x} - \mathbf{x}_{b_j}\right\|) + p(\mathbf{x}), \tag{5}$$

where Φ is a given RBF. Coefficients of the linear polynomial p and α_j are determined by the interpolation conditions:

$$s(\mathbf{x}_{b_j}) = \mathbf{d}_{b_j} \tag{6}$$

$$\sum_{j=1}^{n_b} \alpha_j q(\mathbf{x}_{b_j}) = 0 \tag{7}$$

$\mathbf{d}_{b_j}$ is the imposed displacement of the boundary node $\mathbf{x}_{b_j}$. Equation 7 has to be satisfied for all polynomials q with a degree less or equal than that of polynomial p. In our case, the displacement $\mathbf{d}_{b_j}$ is nullified for all boundary nodes, except the ones belonging to the blade. Independently for each spatial direction, the coefficients of the polynomial p and α_j are recovered solving a $(n_b + 4) \times (n_b + 4)$ symmetric positive definite linear system, using a Cholesky decomposition for instance.
The new position $\mathbf{x}_{new}$ of a node in the interior domain initially located in $\mathbf{x}$ is then directly derived:

$$\mathbf{x}_{new} = \mathbf{x} + s(\mathbf{x}) \tag{8}$$

Each point is moved individually involving that no mesh-connectivity information is needed. The RBF retained in this work is the so-called *Volume* function, with global support, defined by $\Phi(r) = r$. This grid deformation tool is particularly easy to implement, robust, and computationally cheap, so perfectly suitable for the present work.

3.4. Geometry Parametrization

In order to reconstruct the 2D blade profile employing a minimum number of variables, an unique B-spline curve is used to parametrize both pressure and suction sides of the cascade. An exhaustive description of B-splines curves/surfaces can be found in [38] [39]. The approach follows the one successfully applied in [9]. The trailing edge is considered separated from the B-spline, which therefore has to be constrained to pass by the two control points that define the trailing edge, and it is assumed to be a circular arc.

Notations. The following notations will be adopted in this *subsection only*: n, k, P, p, N, x.

A B-spline curve $p(t)$ of degree n can be written as

$$p(t) = \sum_{i=0}^{n} N_{i,k}(t)\mathbf{a}_i, \tag{9}$$

where $\mathbf{a}_i$ denotes the i-th control point (CP) with $i \in [\![0, n]\!]$. $N_{i,k}(t)$ is the corresponding $k-1$ degree polynomial B-Spline basis function, defined recursively by:

$$\begin{aligned} N_{i,1}(t) &= \mathbf{1}_{[t_i, t_{i+1}]}(t) \\ N_{i,k}(t) &= \frac{t - t_i}{t_{i+k-1} - t_i} N_{i,k-1}(t) + \frac{t_{i+k} - t}{t_{i+k} - t_{i+1}} N_{i+1,k-1}(t), \end{aligned} \tag{10}$$

where $\{t_j\}_{j \in [\![0, n+k]\!]}$ denotes the increasing so-called knot sequence, and $t \in [t_{k-1}, t_{n+1}]$ is a scalar parametrising the B-Spline curve.

Properties. We recall some properties on B-splines:

- Polynomial Degree: $p(t)$ is a k degree polynomial curve on $]t_i, t_{i+1}[$.
- Regularity at junction points: $p(t)$ is C^{k-2} at junction points $p(t_i)$.
- Influence Range: CP $\mathbf{a}_i$ affects $p_{[t_i, t_{i+k}]}$.
- Local Control Property: $p_{[t_i, t_{i+1}]}$ is influenced by the k CP $(\mathbf{a}_{i-k+1}, ..., \mathbf{a}_i)$.

Baseline Approximation. The first step is to approximate by a B-Spline curve the baseline geometry represented by $P+1$ data points p_l.
The polynomial degree k, the number of CP and the knot sequence $\{t_j\}_{j \in [\![0, n+k]\!]}$ are user defined.
The CP $\mathbf{a}_i$ can then be estimated minimizing the approximation error defined by:

$$f(x) = \sum_{l=0}^{P} \|p_l - x(\omega_l)\|^2 \tag{11}$$

where x is the B-Spline curve obtained for a given set of control points $\{\mathbf{a}_i\}$. The sequence $\{\omega_l\}$ is computed as the curvilinear abscissae of the points $\{p_l\}_{l \in [\![0, P]\!]}$. $\|.\|$ is the Euclidian distance. Rewriting equation 11 using 9 results in a least squares minimization problem which resolution leads to a linear symmetric system, composed by the following $n+1$ relations:

$$\sum_{i=0}^{n} \mathbf{a}_i \sum_{l=0}^{P} N_{i,k}(\omega_l) N_{j,k}(\omega_l) = \sum_{l=0}^{P} N_{j,k}(\omega_l), \;\; j \in [\![0, n+1]\!]. \tag{12}$$

Each dimensional component of $\mathbf{a}_i$ can be solved independently, by means of Cholesky Decomposition for example. The B-Spline curve is constrained to pass through the first and last data points to create a closed curve along with the circular-shape trailing edge. C^{k-2} regularity is ensured by imposing the first (resp. last) data point to match the first CP $\mathbf{a}_0$ (resp. last CP $\mathbf{a}_n$) by selecting a knot sequence with a so-called multiplicity k at end points, namely $t_0 = ... = t_{k-1}$ (resp. $t_{n+1} = ... = t_{n+k}$).

Choice of knot sequence and impact on parametrization. The knot sequence spacing, namely $\{t_{j+1} - t_j\}_{j \in [\![0, n+k-1]\!]}$, regulates the spacing between the control points, and is chosen following several guidelines: (i) to limit the geometrical error in the reconstruction; (ii) to exploit the non-uniform distribution of CPs, reducing the distance between the CPs in regions of higher curvature; (iii) to limit the CP number in interesting areas for the optimization, thus reducing the

design dimension. In this work, $n + 1 = 30$ CP points are chosen and $k = 3$, resulting in C^1 regularity at junction points and $p(t)$ is polynomial curve of degree 3 on $[t_i, t_{i+1}]$. 11 CPs are allowed to move in the direction normal to the blade (Figure 2), within a predefined range aimed at preventing unfeasible designs and mesh-deformation issues, while ensuring high design flexibility. Note that the displacements of the 4 CPs closest to the trailing edge are linked each other, so that only one CP is movable and the other ones move rigidly with the former; this allows reducing the design dimension while keeping constant geometrical parameters like the thickness and the wedge angle that are important for the structural integrity of the blade.

Fit the parametrization $\bar{\omega}_l$. Once the optimal CP positions $\mathbf{a}_i$ are evaluated solving Equation 12 based on an initial set (possibly large) of data points p_l representing the baseline, the sequence $\bar{\omega}_l$ has to be recovered to match the new set of points $\{\bar{p}_l\}_{l\in[\![0,\bar{P}]\!]}$ defining the blade geometry in the mesh used for optimization purpose. A 1D optimization problem has to be solved for each new point $\bar{p}_l$

$$\bar{\omega}_l = \arg\min_{\omega} \left\| \bar{p}_l - \sum_{i=0}^{n} N_{i,k}(\omega)\mathbf{a}_i \right\|^2, \; l \in [\![0, \bar{P}]\!]. \tag{13}$$

Parametrization Vector $\mathbf{x}$. In the following, $\mathbf{x}$ will denote the vector of normal displacements of the moving CP.

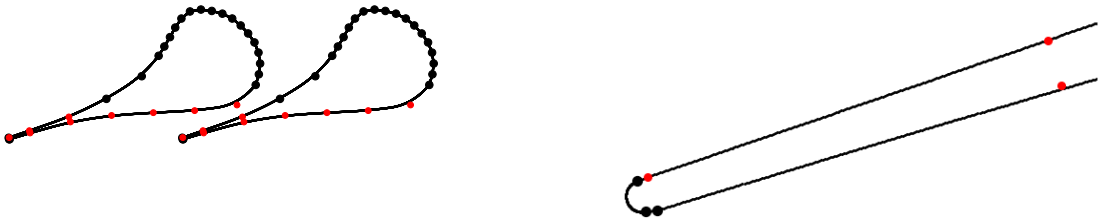

(a) Blade Parametrization

(b) Zoom at Trailing Edge.

Figure 2: Baseline profile approximated by B-splines: 30 CP, 11 Free CP (red), 19 Fixed CP (black).

3.5. Performance assessment of the turbine cascade

In this paper, we focus specifically on two performance parameters. One parameter, ΔP, is defined according to [9] as the standard deviation of the azimuthal pressure distribution evaluated half of an axial chord downstream the blade trailing edge; it is also the targeted quantity used for the optimization. The second performance parameter quantifies the entropy generation in the form of total pressure loss coefficient: $Y = \dfrac{P^t_{in} - P^t_{out}}{P^t_{in} - P^s_{out}}$.

In this work, ΔP and Y are used as objective function in the optimization. Minimizing ΔP within the optimization is convenient for such highly supersonic cascade since it allows achieving a severe reduction of the shock strength, and hence of the shock loss, thus improving the cascade performance and, at the same time, reducing the perturbations entering the downstream rotor. However, also Y is evaluated because a proper analysis of the cascades demands the quantification of an aerodynamic performance parameter.

4. Algorithm Description

Subsection 4.1 discusses the surrogate implementation at the basis of the stochastic and optimization methods, described respectively in Subsection 4.2 and 4.3.

4.1. Gaussian-Process-based Surrogate Model

Surrogate models, a.k.a. meta-models, aim at simulating at low cost a model $\mathcal{M}$ of interest, usually computationally expensive. From a given dataset $\{\mathbf{x}_i, \mathcal{M}(\mathbf{x}_i)\}$, the surrogate is built to approximate the scalar model $\mathcal{M}$. In this study, we employ Gaussian Processes (GP) [40] to represent the quantities of interest, using the library GPy [41] developed in Python. The model of interest is assumed to be a realization of underlying zero mean Gaussian Process Z with the covariance between two sample $\mathbf{x}_i$ and $\mathbf{x}_j$ defined by

$$C_Z(\mathbf{x}_i, \mathbf{x}_j) = \sigma_Z^2 R(\mathbf{x}_i - \mathbf{x}_j, \theta), \tag{14}$$

where σ_Z^2 is the *variance* of the GP and θ a vector of so-called *hyperparameters* driving the so-called *auto-correlation* function R, a.k.a. kernel, such as Gaussian, Matern, or low-order polynomial functions basis. In this work, we use a sum of a first order polynomial and Matern32 kernels. The calibration step consists in identifying the optimal values of θ and σ_Z^2. We use the Maximum Likelihood Estimation technique for identification. The GP approximation at an unknown sample $\mathbf{x}$ is thus given by its *Best Linear Unbiased Estimation* (BLUE, see [42]), which is shown to be a Gaussian random variable $\hat{\mathcal{M}}(\mathbf{x})$:

$$\hat{\mathcal{M}}(\mathbf{x}) \sim \mathcal{N}(\mu_{\hat{\mathcal{M}}(\mathbf{x})}, \sigma_{\hat{\mathcal{M}}(\mathbf{x})}) \tag{15}$$

$\mathcal{N}$ refers to the univariate gaussian law, and $\mu_{\hat{\mathcal{M}}(\mathbf{x})}, \sigma_{\hat{\mathcal{M}}(\mathbf{x})}$ are computed by means of the Gaussian Process algorithm. Further details can be found in [40]. The so-called predictive mean $\tilde{\mathcal{M}}(\mathbf{x}) = \mu_{\hat{\mathcal{M}}(\mathbf{x})}$ is used as a surrogate of $\mathcal{M}(\mathbf{x})$. An epistemic prediction uncertainty characterized by the variance $\sigma^2_{\hat{\mathcal{M}}(\mathbf{x})}$ is also provided. Note that methods presented in this paper are compatible with any meta-model based on GPs, including the Kriging one.

4.2. Uncertainty Quantification (UQ) Methods

Several stochastic techniques are necessary for the present study, and are described in the current Subsection. In the robust optimization process, a quantile of the QoI has to be evaluated efficiently for each design; the techniques here employed for the efficient quantile estimate is discussed in Subsubsection 4.2.2). The optimal profiles are assessed using both inviscid and RANS CFD evaluations, based on LHS experiments in the stochastic space. The variability of scalar random performance parameters is studied in terms of its PDF (Probability Density Function) and statistics, using the techniques discussed in Subsubsection 4.2.1. We also investigate variability distributed on the flow field, in terms of Mach number. In this latter case, due to the large number of QoI involved, a different stochastic approach is considered, presented in Subsubsection 4.2.3.

4.2.1. UQ Surrogated-based: Scalar Statistics Evaluation

Let us introduce the generic random variable $G(\boldsymbol{X})$ where G is a scalar function depending on a random vector $\boldsymbol{X}$ characterized by its so-called joint *Probability Density Function* (PDF) $f_{\boldsymbol{X}}$. In this study, the following statistics of $G(\boldsymbol{X})$ are considered: mean $\mu_G = \mathbb{E}_{\boldsymbol{X}}[G(\boldsymbol{X})]$, standard deviation $\sigma_G = \mathbb{V}_{\boldsymbol{X}}^{\frac{1}{2}}[G(\boldsymbol{X})]$, α-quantile $= q_\alpha^{\boldsymbol{X}}[G(\boldsymbol{X})]$, for $\alpha \in [0, 1]$. We recall their definition here.
The expectation of $G(\boldsymbol{X})$, namely its mean, is defined as:

$$\mathbb{E}_{\boldsymbol{X}}[G(\boldsymbol{X})] = \int G(\mathbf{x}) f_{\boldsymbol{X}}(\mathbf{x}) d\mathbf{x}. \tag{16}$$

The so-called variance of $G(\boldsymbol{X})$ is defined as:

$$\mathbb{V}_{\boldsymbol{X}}[G(\boldsymbol{X})] = \mathbb{E}_{\boldsymbol{X}}[G(\boldsymbol{X})^2] - \mathbb{E}_{\boldsymbol{X}}[G(\boldsymbol{X})]^2. \tag{17}$$

The Coefficient Of Variation (CoV) defined by $\text{CoV} = \frac{\sigma_G}{\mu_G}$ is used to quantify the normalized variability of G, if $\mu_G \neq 0$. The α-quantile $q_\alpha^X[G(\boldsymbol{X})]$ is defined as:

$$q_\alpha^X[G(\boldsymbol{X})] = \inf\{q \in \mathbb{R}\ s.t.\ \mathbb{P}_X(G(\boldsymbol{X}) < q) \leqslant \alpha\}. \tag{18}$$

where $\mathbb{P}_X$ refers to the probability measure relatively to $\boldsymbol{X}$.

An interpretation of the quantile is given through the following example: let us denote with $q_{0.95}^{\boldsymbol{\xi}}[\Delta P(\mathbf{x}, \boldsymbol{\xi})]$, the 95% quantile of $\Delta P(\mathbf{x})$ for a given blade profile parametrized by $\mathbf{x}$. $\Delta P(\mathbf{x})$ is considered as a scalar random variable, whose variability is related to the random vector $\boldsymbol{\xi}$. 95% of the realizations of $\Delta P(\mathbf{x})$ are lower than $q_{0.95}^{\boldsymbol{\xi}}[\Delta P(\mathbf{x}, \boldsymbol{\xi})]$. Otherwise speaking, the probability that $\Delta P(\mathbf{x})$ is lower than $q_{0.95}^{\boldsymbol{\xi}}[\Delta P(\mathbf{x}, \boldsymbol{\xi})]$ equals 95%, *i.e.* $\mathbb{P}_{\boldsymbol{\xi}}(\Delta P(\mathbf{x}) < q_{0.95}^{\boldsymbol{\xi}}[\Delta P(\mathbf{x}, \boldsymbol{\xi})]) = 0.95$.

In order to compute all these statistics accurately, surrogate model and Monte Carlo techniques are used. Based on a Design of Experiment (DOE) using Latin Hypercube Sampling (LHS) where the performance function G is evaluated, a surrogate $\tilde{G}$ is built (Subsection 4.1). A large Monte Carlo Sampling (MCS) is then drawn and evaluated by means of the surrogate in order to estimate empirically the statistics. Stochastic convergence is assessed *a-posteriori*, estimating the statistics for different DOE sizes. The detailed steps are the following:

1. Build a DOE (LHS) and evaluate the performance function G at each sample, yielding: $\{\mathbf{x}_j^0, G(\mathbf{x}_j^0)\}_{j \in [\![1, N_{LHS}]\!]}$, where $\mathbf{x}_j^0$ refers to a realization of the random vector $\boldsymbol{X}$.
2. Build a GP surrogate from the DOE: $\tilde{G}$
3. Sample a large MC set: $\{\mathbf{x}_k\}_{k \in [\![1, N_{MC}]\!]}$
4. Compute MC empirical mean, variance, and α-quantile: respectively $\hat{\mu}_{\tilde{G}}$, $\hat{\sigma}^2_{\tilde{G}}$, and $\hat{q}_\alpha^{\tilde{G}}$ based on the surrogate $\tilde{G}$, considering the set $\{\tilde{G}(\mathbf{x}_k)\}_k$ sorted:

$$\hat{\mu}_{\tilde{G}} = \frac{1}{N_{MC}} \sum_{k=1}^{N_{MC}} \tilde{G}(\mathbf{x}_k) \tag{19}$$

$$\hat{\sigma}^2_{\tilde{G}} = \frac{1}{N_{MC}} \sum_{k=1}^{N_{MC}} (\tilde{G}(\mathbf{x}_k) - \hat{\mu}_{\tilde{G}})^2 \tag{20}$$

$$\hat{q}_\alpha^{\tilde{G}} = \tilde{G}(\mathbf{x}_{\lceil \alpha N_{MC} \rceil}) \tag{21}$$

Concerning the mean, its estimate is the most obvious calculation and does not require a specific treatment, once the GP-surrogate for the QoI has been obtained. The method is summarized in Algorithm 1.

Algorithm 1: Mean Estimation

Input: N_{LHS}, N_{MC}

1 Initial DoE: $\{\mathbf{x}_j, G(\mathbf{x}_j)\}_{j \in [\![1, N_{LHS}]\!]}$;
2 Build GP Metamodel: $\tilde{G}$;
3 Mean Estimation using Equation 19 and N_{MC} MC samples ;

4.2.2. Efficient Quantile Estimation

For each given blade profile parametrized by a design vector $\mathbf{x}$, the 95-quantile $q_{95}^{\boldsymbol{\xi}}[\Delta P(\mathbf{x}, \boldsymbol{\xi})]$ of the random variable $\boldsymbol{\xi} \to \Delta P(\mathbf{x}, \boldsymbol{\xi})$, where $\boldsymbol{\xi}$ denotes the random vector of the input uncertainties, needs to be accurately evaluated. The algorithm proposed is very similar to the one in [24]. For a sake of clarity, the algorithm is described for the generic problem of evaluating the quantile q of level $\alpha \in [0, 1]$ for the (expensive) scalar performance function $G(\boldsymbol{X})$, where $\boldsymbol{X}$ is a random vector of $\mathbb{R}^d$ characterized by its joint PDF $f_{\boldsymbol{X}}$: $\mathbb{P}_X(G(\boldsymbol{X}) < q) = \alpha$.

The algorithm can be divided in three main steps:

1. Set an initial DOE and build an initial surrogate $\tilde{G}$.

2. Select a batch of K candidates based on the current $\tilde{G}$ knowledge. Evaluate the K samples. Update $\tilde{G}$.
3. Repeat Step 2 until a stopping criterion is satisfied.

Initial DOE. An initial DOE of size N_{LHS} is generated using LHS. A slight modification is done w.r.t. the original algorithm [24]: an iso-probabilistic transformation T (e.g. Rosenblatt or Nataf transform) is used to perform the LHS in the standard space, namely a space where all variables are independently and normally distributed with zero mean and unit variance. More specifically, we write $\boldsymbol{U} = T(\boldsymbol{X})$, where $\boldsymbol{U} \sim \mathcal{N}(0, I_d)$ is the standard normal random vector of $\mathbb{R}^d$. N_{LHS} samples of the random vector $\boldsymbol{U}$ are generated by means of LHS in $[a_{min}, a_{max}]^d$: $\{\boldsymbol{u}_k\}_{k\in[\![1,N_{LHS}]\!]}$. The performance function G is then evaluated on the *physical samples* $\{\mathbf{x}_k\}_{k\in[\![1,N_{LHS}]\!]}$, defined as $\mathbf{x}_k = T^{-1}(\boldsymbol{u}_k)$. A first surrogate $\tilde{G}$ is built from this DOE. This modification aims at generating samples in regions of low probability. a_{min} and a_{max} should be set in good agreement with the target quantile level α. We propose the following rule of thumb:

$a_{max} = -a_{min} = \Phi^{-1}(\max(1-\alpha, \alpha))$, Φ denoting the so-called *cumulative density function* of the univariate gaussian law.

Batch Selection. In cases where parallel computing is available, it can be beneficial to add multiple points at the same time to speed up the overall computation even if the procedure may be slightly suboptimal. K samples are determined at the beginning of each iteration, the corresponding model responses being evaluated computed simultaneously on K independent CPUs. More details can be found in [24].

Stopping Criterion. The adaptive sampling strategy described in the previous paragraph is performed until the following criterion is satisfied

$$\frac{q^+ - q^-}{q_{ref}} \leqslant \epsilon \tag{22}$$

where ϵ is a small value, typically 5% and q_{ref} is a normalization quantity that can also be set to q, the current quantile estimate; q^+ and q^- are bounds estimates of the quantile, using the gaussian nature of the surrogate [24]. In cases where the quantile q is totally unknown and can be close to zero, a suitable normalization constant could be σ_G, the empirical standard deviation of $G(\boldsymbol{X})$ [24]. In this paper, q_{ref} is set to the QOI ΔP at nominal condition for the baseline profile. If the relationship 22 holds, the surrogate is considered to be accurate enough for the quantile estimation. The tuning parameters related to the efficient surrogate-based quantile estimation used here are summarized in Table 3.

N_{LHS}	a_{max}	N_{MC}	K	ϵ	q_{ref}
8	2	10^6	8	0.05	$\Delta P_{baseline}$

Table 3: Tuning Parameters for the Surrogate-based Quantile Estimation

The method is summarized in the Algorithm 2.

Algorithm 2: Efficient Quantile Evaluation

Input: N_{LHS}, ϵ, q_{ref}, $G : \mathbb{R}^d \to \mathbb{R}$
Initial DoE: $\{\mathbf{x}_j, G(\mathbf{x}_j)\}_{j\in[\![1,N_{LHS}]\!]}$;
Build GP Metamodel: $\tilde{G}$;
Estimation q^+, q^-, q ;
while $\frac{q^+ - q^-}{q_{ref}} \leqslant \epsilon$ **do**
    Selection K samples [24]: $\{\bar{\mathbf{x}}_1, ..., \bar{\mathbf{x}}_K\}$;
    Evaluation: $\{G(\bar{\mathbf{x}}_1), ..., G(\bar{\mathbf{x}}_K)\}$;
    Update Metamodel ;
    Estimation q^+, q^-, q
Return q ;

4.2.3. PCA-UQ Surrogated-based: Vector Statistics Evaluation

We are interested in evaluating efficiently statistics where the quantity of interest is a vector, possibly with a large dimension (say 10^5). As a consequence, the method presented in Subsubsection 4.2.1 is not tractable, since it would require to build a large number of surrogate models.
Let us consider the generic random variable $\boldsymbol{G}(\boldsymbol{X})$ where $\boldsymbol{G} : \mathbb{R}^d \to \mathbb{R}^n$ is a multidimensional function depending on a random vector $\boldsymbol{X}$ characterized by its PDF $f_{\boldsymbol{X}}$. In the following, we describe a stochastic method combining a PCA (Principal Component Analysis) decomposition to reduce the dimension space n, surrogate modeling and MC sampling. Below, a summary of the method:

1. Set an initial DOE: Data generation using LHS.
2. PCA: compute the eigenmodes, and select the most energetic ones.
3. Build a surrogate of each scalar coefficient in the reduced basis.
4. MC sampling on the scalar coefficients.
5. Recover the statistics of $\boldsymbol{G}$

Initial DOE. As in Subsubsection 4.2.1, N_{LHS} samples using LHS are generated, then stored in the mean subtracted data matrix $Y = [\boldsymbol{G}(\mathbf{x}_i)^{(j)} - \boldsymbol{\mu}_G^{(j)}]_{ij} \in \mathbb{R}^{N_{LHS} \times n}$. $\boldsymbol{\mu}_G \in \mathbb{R}^n$ denotes the data empirical mean, defined as $\boldsymbol{\mu}_G^{(j)} = \frac{1}{N_{LHS}} \sum_{k=1}^{N_{LHS}} \boldsymbol{G}(\mathbf{x}_i)^{(j)}$. $\boldsymbol{G}(\mathbf{x}_i)^{(j)}$ is the j-th component of the vector $\boldsymbol{G}(\mathbf{x}_i) \in \mathbb{R}^n$. Mean subtraction is an integral part of the solution towards finding a principal component basis minimizing the data approximation mean square error [43].

PCA and modes selection. The semi-definite positive empirical covariance matrix is built:

$$C = \frac{Y^T Y}{N_{LHS} - 1} \tag{23}$$

$C \in \mathbb{R}^{n \times n}$ is then decomposed into an orthogonal basis of eigenvectors $\boldsymbol{V} = (\boldsymbol{v}_1, ..., \boldsymbol{v}_n)$, involving $\boldsymbol{v}_i^T \boldsymbol{v}_j = \delta_{ij}$, as

$$C = V \Lambda V^T \tag{24}$$

$\Lambda = diag(\lambda_1, ..., \lambda_n)$ is a diagonal matrix where the positive eigenvalues are sorted in decreasing order. L modes are retained based on the following cumulative energy eigenmodes criterion:

$$L = \arg\min\{l \in [\![1, n]\!] \text{ s.t. } \frac{\sum_{i=1}^{l} \lambda_i}{\sum_{i=1}^{n} \lambda_i} > \Delta\} \tag{25}$$

where $\Delta \leq 1$ is a threeshold value close to 1, $\frac{\sum_{i=1}^{l} \lambda_i}{\sum_{i=1}^{n} \lambda_i}$ represents the normalized cumulative energy associated to the l first modes. The closer the threeshold is to 1, the more modes are selected and the more accurate the approximation is. Note that in the cases that we consider, $N_{LHS} << n$, so the covariance matrix C has a rank N_{LHS} at maximum so $l \leq N_{LHS}$. The l eigenvectors $\{\boldsymbol{v}_k\}_{k \in [\![1,l]\!]}$ with $\boldsymbol{v}_k \in \mathbb{R}^n$ are set are basis vectors, the vector solution $\boldsymbol{G}(\mathbf{x})$ at an unknown location $\mathbf{x}$ is sought in the form

$$\boldsymbol{G}(\mathbf{x}) - \boldsymbol{\mu}_G = \sum_{i=1}^{l} h_i(\mathbf{x}) \boldsymbol{v}_i \tag{26}$$

where $h_i(\mathbf{x})$ are the scalar coefficients in the reduced basis, which need to be approximated by a surrogate. The following DOE is used to build the surrogates $\tilde{h}_i$: $\{\mathbf{x}_k, \boldsymbol{v}_i^T (\boldsymbol{G}(\mathbf{x}_k) - \mu_G)\}_{k \in [\![1, N_{LHS}]\!]}$. A surrogate for $\boldsymbol{G}$ consequently reads

$$\tilde{\boldsymbol{G}}(\mathbf{x}) = \sum_{i=1}^{l} \tilde{h}_i(\mathbf{x}) \boldsymbol{v}_i + \boldsymbol{\mu}_G \tag{27}$$

Mean and Variance. The decomposition in the reduced basis (Equation 26) is used to approximate the random vector. From the linearity of the operator $\mathbb{E}_{\boldsymbol{X}}$, we obtain:

$$\mathbb{E}_{\boldsymbol{X}}[\boldsymbol{G}(\boldsymbol{X})] = \boldsymbol{\mu}_G + \sum_{i=1}^{l} \mu_{h_i} \boldsymbol{v}_i \tag{28}$$

where $\mu_{h_i} = \mathbb{E}_{\boldsymbol{X}}[h_i(\boldsymbol{X})]$ denotes the mean of the coefficient h_i. The variance of $\boldsymbol{G}(\boldsymbol{X})$ is derived by component $j \in [\![1, n]\!]$, since they are uncorrelated w.r.t. the random vector $\boldsymbol{X}$:

$$\begin{aligned} \mathbb{V}_{\boldsymbol{X}}[\boldsymbol{G}(\boldsymbol{X})^{(j)}] &= \mathbb{V}_{\boldsymbol{X}}[\sum_{i=1}^{l} h_i(\boldsymbol{X}) \boldsymbol{v}_i^{(j)}] \\ &= \sum_{i=1}^{l} \boldsymbol{v}_i^{(j)} \boldsymbol{v}_i^{(j)} \sigma_{h_i}^2 + 2 \sum_{i=1}^{n} \sum_{k=i+1}^{n} \boldsymbol{v}_i^{(j)} \boldsymbol{v}_k^{(j)} \rho_{ik} \end{aligned} \tag{29}$$

where $\sigma_{h_i}^2 = \mathbb{V}_{\boldsymbol{X}}[h_i(\boldsymbol{X})]$ and $\rho_{ik} = \mathbb{E}_{\boldsymbol{X}}[h_i(\boldsymbol{X}) h_k(\boldsymbol{X})] - \mu_{h_i} \mu_{h_k}$ denote respectively the variance of h_i and the covariance between h_i and h_k. This derivation (Equation 29) takes into account that the coefficients h_i can be correlated.

μ_{h_i}, $\sigma_{h_i}^2$, ρ_{ik} are evaluated numerically by means of MC on the metamodels $\tilde{h}_i$ so the mean (resp. variance) of $\tilde{\boldsymbol{G}}(\boldsymbol{X})$ are easily reconstructed using Equation 28 (resp. Equation 29).

Numerical Aspects. Note that in practice, the eigen-decomposition $(\Delta, \boldsymbol{V})$ is not obtained by evaluating the covariance matrix C and then perform the diagonalization as suggested by Equation 24. Indeed, $C \in \mathbb{R}^{n \times n}$ can be very large and ill-conditioned since $\text{cond}(C) = \text{cond}(Y)^2$.
A Singular Value Decomposition (SVD) on the mean subtracted data matrix Y is preferred, yielding

$$Y = \boldsymbol{U} \Sigma \boldsymbol{V}^T \tag{30}$$

$\boldsymbol{U} \in \mathbb{R}^{N_{LHS} \times N_{LHS}}$ is an orthonormal matrix with the property $\boldsymbol{U}^T \boldsymbol{U} = I_{N_{LHS}}$. $\Sigma \in \mathbb{R}^{N_{LHS} \times n}$ is a *diagonal matrix* of eigenvalues $\{\sigma_k\}_k$. Equation 30 is justified by

$$\begin{aligned} C &= \frac{(\boldsymbol{U} \Sigma \boldsymbol{V}^T)^T \boldsymbol{U} \Sigma \boldsymbol{V}^T}{N_{LHS} - 1} \\ &= \boldsymbol{V} \frac{\Sigma^T \Sigma}{N_{LHS} - 1} \boldsymbol{V}^T \end{aligned} \tag{31}$$

Equation 31 also reveals the underlying relation between eigenvalues of matrices C and Y:

$$\lambda_i = \frac{\sigma_i^2}{N_{LHS} - 1} \tag{32}$$

4.3. Framework for Surrogate-based Design Optimization

We perform four different optimizations in this study. The first two ones are under a deterministic constraint: one based on the inviscid flow model and aimed at minimizing ΔP and the other based on the RANS flow model and using Y as QoI. For both cases, the mass flow rate is the constraint function. Note that in the RANS-based optimization, the fitness function to optimize is Y and not ΔP, since this is a more traditional choice for RANS optimization. This case is introduced as a benchmark for illustrating the usefulness of using an inviscid model for driving the optimization, which could yield optimal design with efficient performances also for RANS simulations. The RANS-based optimization is made feasible by the relatively low cost of the deterministic formulation. The algorithmic details for deterministic optimization are given in Subsection 4.3.1.

The two latter are robust optimizations, using the inviscid flow model, with the following formulations: the first one is based on a classical formulation, and it is focused on the minimization of the mean of ΔP (See Subsubsection 4.3.2); the second one is based on the novel approach proposed in this paper, and aims at minimizing the 95% quantile of ΔP (See Subsubsection 4.3.3). Both the robust optimizations are formulated under a mean-based probabilistic constraint on the mass flow rate.

4.3.1. Constrained Deterministic Optimization

For an n-dimensional problem, we are concerned with solving the following single-objective optimization problem:

$$\begin{aligned} &\text{Minimize} \quad f(\mathbf{x}) \\ &\quad \text{s.t.} \quad g(\mathbf{x}) \in [g_{min}, g_{max}] \\ &\qquad \mathbf{x} \in \Omega \end{aligned} \tag{33}$$

where f and g denote respectively the objective and constraint functions, and $\mathbf{x}$ is the vector of design variables corresponding to a blade parametrization, Ω being the design space, tensor product of intervals defined by upper and lower limits of each component of $\mathbf{x}$.

We employ a classic bayesian framework for Surrogate-Based Optimization (SBO):

1. Set an initial DOE and build initial surrogates for the objective and the constraint functions.
2. Generate a new design solving a sub-optimization problem based on the surrogates. It aims at either further explore the design space or exploit a promising region. The new design is evaluated by means of the original objective function y (CFD). Surrogate models are updated.
3. Repeat Step 2 until a stopping criterion is satisfied or a maximal evaluation budget is reached.

A general sketch of the proposed framework for tackling robust optimization problems is provided in Figure 3.

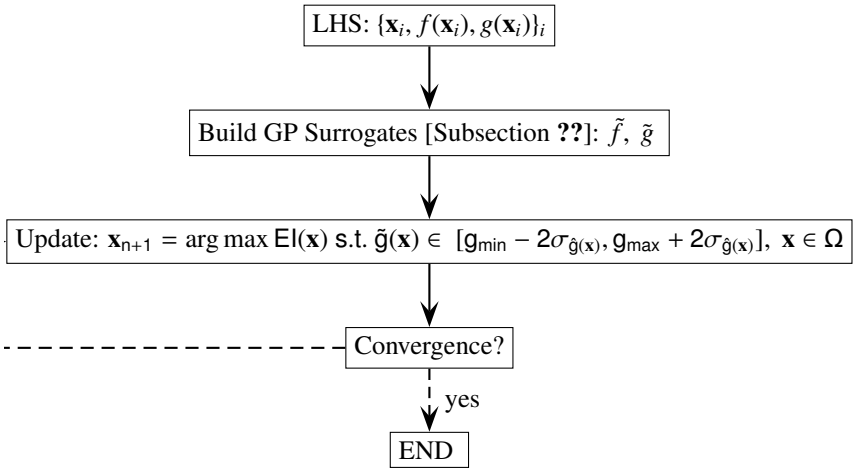

Figure 3: General Sketch of the Expected Improvement [25]-based algorithm used for Deterministic Optimization (Eq. 2).

Initial DOE. An initial DOE of size $N^{\mathbf{x}}_{LHS}$ is generated using LHS over the design space $[\mathbf{x}_{min}, \mathbf{x}_{max}]$, for which the objective and constraint functions are evaluated (CFD): $\{\mathbf{x}_i, f(\mathbf{x}_i), g(\mathbf{x}_i)\}_{i \in [\![1, N^{\mathbf{x}}_{LHS}]\!]}$. Surrogates of f and g are then built (Subsection 4.1).

Sample Infill Criterion and Sub-optimization. We focus on one of the most popular criterion in Efficient Global Optimization (EGO) [25]: the Expected Improvement (EI).

For a given untried sample $\mathbf{x}$, the Improvement is defined as

$$I(\mathbf{x}) = max(0, f_{min} - \hat{f}(\mathbf{x})), \tag{34}$$

f_{min} denoting the minimum objective function value observed so far. $\hat{f}(\mathbf{x})$ is the gaussian predictor of the GP based surrogate of f at the sample $\mathbf{x}$. Note that $I(\mathbf{x})$ is a random scalar value which is positive when the prediction is lower

than the best value known thus far, set to 0 otherwise. The new query point is found by maximizing the expected improvement:

$$\mathbf{x}^* = \arg\max EI(\mathbf{x}) \tag{35}$$

$EI(\mathbf{x}) = \mathbb{E}_{\hat{f}(\mathbf{x})}[I(\mathbf{x})]$ denotes the so-called *Expected Improvement* at $\mathbf{x}$, whose analytical expression is given by [25]:

$$\begin{aligned} EI(\mathbf{x}) =& (\mu_{\hat{f}(\mathbf{x})} - f_{min})\Phi(Z) + \sigma_{\hat{f}(\mathbf{x})}\phi(Z) && \text{if } \sigma_{\hat{f}(\mathbf{x})} > 0 \\ =& 0 && \text{if } \sigma_{\hat{f}(\mathbf{x})} = 0 \end{aligned} \tag{36}$$

$Z = \dfrac{\mu_{\hat{y}(\mathbf{x})} - y_{min}}{\sigma_{\hat{y}(\mathbf{x})}}$, Φ (resp. ϕ) is the univariate gaussian standard cumulative (resp. probability) density function.

The original EI infill criterion [25] in Equation 35 is slightly modified in order to take into account for the constraint. The new query point thus reads:

$$\begin{aligned} \mathbf{x}^* &= \arg\max EI(\mathbf{x}) \\ &\text{s.t. } \tilde{g}(\mathbf{x}) \in [g_{min} - 2\sigma_{\hat{g}(\mathbf{x})}, g_{max} + 2\sigma_{\hat{g}(\mathbf{x})}] \\ &\mathbf{x} \in \Omega \end{aligned} \tag{37}$$

The sub-optimization problem Equation 37 can be solved by means of any gradient-free optimizer, e.g. using Covariance Matrix Adaptation (CMA) [44] in Python. $\mathbf{x}^*$ is then evaluated with CFD, and surrogate models are updated.

The bayesian optimization framework is summarized in Algorithm 3 for a sake of clarity.

Algorithm 3: Bayesian Optimization

Input: $N^{\mathbf{x}}_{LHS}$, $N^{\mathbf{x}}$

$N^{\mathbf{x}}_{LHS}$ samples: $\{\mathbf{x}_i, f(\mathbf{x}_i), g(\mathbf{x}_i)\}_i$;
Build GP and EI (Eq. 36): $\tilde{f}(\mathbf{x})$, $\tilde{g}(\mathbf{x})$, $EI(\mathbf{x})$;
$i = N^{\mathbf{x}}_{LHS}$;
while $i < N^{\mathbf{x}}$, **do**
    Selection: $\mathbf{x}_{i+1} = \arg\max EI(\mathbf{x})$ s.t. $\tilde{g}(\mathbf{x}) \in [g_{min} - 2\sigma_{\hat{g}(\mathbf{x})}, g_{max} + 2\sigma_{\hat{g}(\mathbf{x})}]$, $\mathbf{x} \in \Omega$;
    Evaluation: $f(\mathbf{x}_{i+1}), g(\mathbf{x}_{i+1})$;
    Update GP, EI ;
    $i \leftarrow i + 1$
Return $\mathbf{x}_i$;

4.3.2. Robust Optimization: Mean Minimization

We describe the approach used to perform the following classical mean robust optimization:

$$\begin{aligned} \text{Minimize } & \mathbb{E}_{\boldsymbol{\xi}}[f(\mathbf{x}, \boldsymbol{\xi})] \\ \text{s.t. } & \mathbb{E}_{\boldsymbol{\xi}}[g(\mathbf{x}, \boldsymbol{\xi})] \in [g_{min}, g_{max}] \\ & \mathbf{x} \in \Omega \end{aligned} \tag{38}$$

where f and g are scalar random functions, f representing the objective to minimize and g the constraint. $\boldsymbol{\xi}$ is the random vector, and $\mathbf{x}$ is the vector of design variables. A very similar approach w.r.t. the robust optimization consisting in minimizing a quantile is considered, the only difference consisting in computing the estimation $e_f(\mathbf{x})$ of the mean $\mathbb{E}_{\boldsymbol{\xi}}[f(\mathbf{x}, \boldsymbol{\xi})]$, for each design sample $\mathbf{x}$ using the surrogate-based method described in Subsubsection 4.2.1 based on $N^{\boldsymbol{\xi}}_{LHS} = 24$ LHS samples. The LHS sample size is selected based on stochatic convergence study not shown here for a sake of brevety.

The method is summarized in Algorithm 4, based on the mean estimation recalled in Algorithm 1.

Algorithm 4: Robust Optimization: Mean Formulation

Input: $N^{\mathbf{x}}_{LHS}$, $N^{\mathbf{x}}$, $N^{\boldsymbol{\xi}}_{LHS}$, N_{MC}

Sample $N^{\mathbf{x}}_{LHS}$ LHS profiles: $\{\mathbf{x}_i\}_i$;

Evaluate Means $e_f(\mathbf{x}_i)$, $e_g(\mathbf{x}_i)$: Algorithm 1 with $N^{\boldsymbol{\xi}}_{LHS}$, N_{MC} ;

Build GP and EI (Eq. 36): $\tilde{q}_f(\mathbf{x})$, $\tilde{e}_g(\mathbf{x})$;

$i = N^{\mathbf{x}}_{LHS}$;

while $i < N^{\mathbf{x}}$ **do**

  Selection: $\mathbf{x}_{i+1} = \arg\max EI(\mathbf{x})$ s.t. $\tilde{e}_g(\mathbf{x}) \in [g_{min} - 2\sigma_{\hat{e}_g(\mathbf{x})}, g_{max} + 2\sigma_{\hat{e}_g(\mathbf{x})}]$;

  Evaluate Means $e_f(\mathbf{x}_{i+1})$, $e_g(\mathbf{x}_{i+1})$: Algorithm 1 with $N^{\boldsymbol{\xi}}_{LHS}$ samples Update GP and EI ;

  $i \leftarrow i + 1$

The parameters related to the constrained deterministic/robust optimization used here are summarized in Table 4.

n	$N^{\mathbf{x}}_{LHS}$	$N^{\boldsymbol{\xi}}_{LHS}$	$\dot{m}_{min}$ [%]	$\dot{m}_{max}$ [%]	N	$N^{\mathbf{x}}$
9	$5n$	24	98	102	10^6	300

Table 4: Parameters for the Deterministic and Robust Optimizations (Subsubsection 4.3.1 and 4.3.3).

4.3.3. Robust Optimization: Quantile Minimization

Here we are concerned with solving the following single-objective optimization problem:

$$\begin{aligned} &\text{Minimize } q^{\boldsymbol{\xi}}_{95}[f(\mathbf{x},\boldsymbol{\xi})] \\ &\quad \text{s.t. } \mathbb{E}_{\boldsymbol{\xi}}[g(\mathbf{x},\boldsymbol{\xi})] \in [g_{min}, g_{max}] \\ &\quad\quad \mathbf{x} \in \Omega \end{aligned} \tag{39}$$

where f and g are scalar random functions, f representing the objective to minimize and g the constraint. $\boldsymbol{\xi}$ is the random vector, and $\mathbf{x}$ is the vector of design variables.

To solve this optimization problem, we propose a nested approach combining the SBO framework described in Subsubsection 4.3.1, and the UQ tools described in Subsection 4.2:

- For each design sample $\mathbf{x}_0$, the estimation $q_f(\mathbf{x}_0)$ of the 95-quantile $q^{\boldsymbol{\xi}}_{95}[f(\mathbf{x}_0,\boldsymbol{\xi})]$ is carried out running CFD evaluations in the *stochastic space* (Algorithm 2), the latters being used to evaluate the estimation $e_g(\mathbf{x}_0)$ of the mean $\mathbb{E}_{\boldsymbol{\xi}}[g(\mathbf{x}_0,\boldsymbol{\xi})]$ (Algorithm 1).
- The functions $q_f(\mathbf{x})$ and $e_g(\mathbf{x})$ are directly plugged-in the SBO framework described in Subsubsection 4.3.1.

The present method is summarized in Algorithm 5.

Algorithm 5: Robust Optimization: Quantile Formulation

Input: $N^{\mathbf{x}}_{LHS}$, $N^{\boldsymbol{\xi}}_{LHS}$, $N^{\mathbf{x}}$, ϵ, q_{ref}

Sample $N^{\mathbf{x}}_{LHS}$ profiles: $\{\mathbf{x}_i\}_i$;

Evaluate Quantile $q_f(\mathbf{x}_i)$: Algorithm 2 with inputs $N^{\boldsymbol{\xi}}_{LHS}$, ϵ, q_{ref}, $f(\mathbf{x}_i,\cdot)$;

Evaluate Mean $e_g(\mathbf{x}_i)$: Algorithm 1;

Build GP and EI (Eq. 36): $\tilde{q}_f(\mathbf{x})$, $\tilde{e}_g(\mathbf{x})$;

$i = N^{\mathbf{x}}_{LHS}$;

while $i < N^{\mathbf{x}}$ **do**

  Selection: $\mathbf{x}_{i+1} = \arg\max EI(\mathbf{x})$ s.t. $\tilde{e}_g(\mathbf{x}) \in [g_{min} - 2\sigma_{\hat{e}_g(\mathbf{x})}, g_{max} + 2\sigma_{\hat{e}_g(\mathbf{x})}]$;

  Evaluate Quantile $q_f(\mathbf{x}_{i+1})$: Algorithm 2 with inputs N^{θ}_{LHS}, ϵ, q_{ref}, $f(\mathbf{x}_{i+1},\cdot)$, $\mathbf{x} \in \Omega$;

  Evaluate Mean $e_g(\mathbf{x}_{i+1})$: Eq. 19 Update GP and EI ;

  $i \leftarrow i + 1$

5. Results

The capabilities of the methods described in Section 4 are demonstrated by redesigning the supersonic cascade first investigated in [26] and optimized under deterministic assumptions in [5], [9], and [6]. Four formulations are compared:

- *Euler-Based Deterministic Optimization*: the blade is optimized considering fixed operating conditions (nominal design point, as defined in Table 2) under the constraint of preserving the baseline mass-flow within a 2% range. This case is performed following the deterministic optimization algorithm described in Subsubsection 4.3.1, based on inviscid simulations where the QoI is ΔP. The resulting profile is referred to as the *O-E* profile.
- *RANS-Based Deterministic Optimization*: this case is similar to the former, but based on RANS simulations where the QOI is Y. The resulting profile is referred to as the *O-NS* profile.
- *Robust Optimization - Mean Formulation*: This case accounts for the environmental variability modeled by a random vector $\boldsymbol{\xi}$ (as defined in Table 2), using a classic robust optimization formulation, namely minimizing the QoI mean using the method described in Subsubsection 4.3.2, under the constraint of preserving the mean mass-flow rate within 2% of the baseline value. This profile is referred to as the *RO-E-*μ profile and is based on inviscid simulations.
- *Robust Optimization - Quantile Formulation*: This optimization also accounts for environmental variability modeled by a random vector $\boldsymbol{\xi}$ (as defined in Table 2), solving the quantile-based optimization problem described in Subsubsection 4.3.3, referring to the 95% quantile, under the constraint of preserving the mean mass-flow rate within 2% of the baseline value. This profile is referred to as the *RO-E-*q_{95} profil and is based on inviscid simulations.

ΔP is the best candidate as QoI for the euler-based optimization of this cascade, for several reasons. Previous studies [5, 26] indicate that the baseline cascade features a strong shock released downstream, whose mixing contributes significantly to the loss generation. Minimizing ΔP means primarily to minimize the shock losses, and hence indirectly to minimize the impact of shock-boundary layer interaction. Moreover, differently from Y, ΔP is properly quantified by both the inviscid and the RANS models, and hence it is more suitable for the present study as most of the optimizations performed are based on inviscid simulations. Finally, minimizing ΔP is also beneficial for the subsequent rotor aerodynamics, as a more uniform pressure field at the rotor inlet implies a lower stator-rotor interaction and, hence, a weaker rotor aerodynamic forcing, that in transonic/supersonic turbine might produce relevant performance degradation [45, 46].

The optimal profiles that we obtained from the various optimizations are systematically compared with each other using the high-fidelity RANS solver.

This section is organized as follows. A preliminary study about mesh and statistics convergence is presented in Section 5.1. In Sections 5.2 the results of the optimization are documented: convergence, geometry profiles, mesh deformation, UQ assessment, the comparison between RANS and inviscid based results are discussed. In Subsection 5.5, a physical analysis of the optimized cascades is performed.

5.1. Mesh and statistics convergence

The spatial resolution of the computational mesh is selected as a result of a dedicated grid dependence study, based on the two performance parameters previously introduced, *i.e.* ΔP and Y.

In the following analysis, the robust optimizations are performed using the inviscid model, whereas the deterministic optimizations and the *a-posteriori* assessment of all the optimal individuals are performed using both the inviscid and the high-fidelity (RANS) model. Therefore, two different grid dependence analyses are carried out, and two alternative mesh resolutions are ultimately adopted for the two models. They are discussed separately in the following.

Euler Analysis. The grid sensitivity analysis for the inviscid simulations is carried out considering ΔP only as QoI. This is motivated by the fact that the value of Y is of limited quantitative relevance in inviscid models (in such simulations the viscous contribution only depends on the artificial viscosity). Figure 4(a) reports the percentage

errors of 5 different meshes, the most refined one (250 kcells) is taken as reference. The trend shows that the grid dependence of the solutions obtained using meshes composed by 36 kcells or more is relatively low (below 1% difference with respect to the reference), with the mesh composed by 112 kcells very close to the reference one (0.3% difference with respect to the reference). In light of these results, the 36 kcell mesh is considered to provide the best trade-off between computational cost and accuracy; the reliability of the 36 kcell mesh is further demonstrated by the pressure distribution along the blade sides, which reproduces with good accuracy the one obtained with the reference mesh as reported in Figure 4(b). Therefore, the 36k mesh is employed to carry out the deterministic and robust optimization procedures. For the *a-posteriori* UQ analysis performed with inviscid flow assumption, lower restrictions in computational cost hold and the 112 kcell grid is employed. Still regarding the inviscid UQ analysis, different LHS sets (dimension 50, 100, 150) are considered to compute the performances of the blade. Results show that the convergence on the statistical quantities is reached with a LHS of dimension 100.

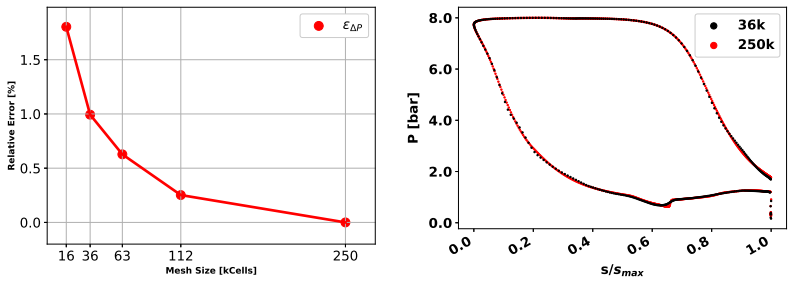

(a) (b)

Figure 4: Euler Grid Analysis at Nominal Conditions on the baseline configuration. (a) ΔP Relative Error, (b) Pressure Distribution comparison between 36k and 250k cells meshes.

RANS Analysis. High-fidelity simulations based on the RANS model are used to perform a benchmark deterministic optimization and are employed to assess the performances of all the optimized profiles. A grid analysis is again performed, to properly set the mesh spatial discretization, for meshes ranging from 52 kcells to 590 kcells, with this latter taken as reference. Figure 5(a) reports the percentage error computed on the performance estimators ΔP and Y. Given the good compromise between accuracy and computational cost, the 180k cells mesh is retained to compute the blade performances in the UQ framework, while the 52k cells mesh is retained in the optimization procedure for solving Eq. 1. Figure 5(b) plots the pressure distribution over the blade as resulting from using the 180k and the 590k elements mesh.

The performance statistics of the baseline profile are evaluated by performing an UQ analysis using LHS (off-design experiments) of dimension 50, 100 and 150. The PDF of Y (Total pressure loss) is plot (Figure 5)(c): the stochastic convergence is satisfactory reached with a LHS size of 100. The results of this post-processing procedure are described in Subsubsections 4.2.1 4.2.3.

5.2. Optimization Process

All the optimization problems are started with DOE consisting in $5d = 45$ profiles, the design space dimension being $d = 9$. The influence of the number of initial sample designs (in the context of bayesian deterministic optimization) has been studied by Han et al. [47], along with the effect of randomness of the initial sampling (considering five LHS samples of the same size generated with different seeds). For 40 design variables, as a rule of thumb, they suggested to use between $0.5d$ and $2d$ as the size of the initial DOE, and found very similar convergence histories for the different LHS seeds. In the present study, we decided to exceed significantly with the DOE size ($5d$) with respect to the recommendations reported in [47], with the aim of enhancing the reliability of the surrogate optimization.

After the DOE, the EI optimization algorithm stops after a maximal number of runs (300) or if the same designs (or very close) are proposed by the optimizer. A review of the optimization processes is reported in this section.

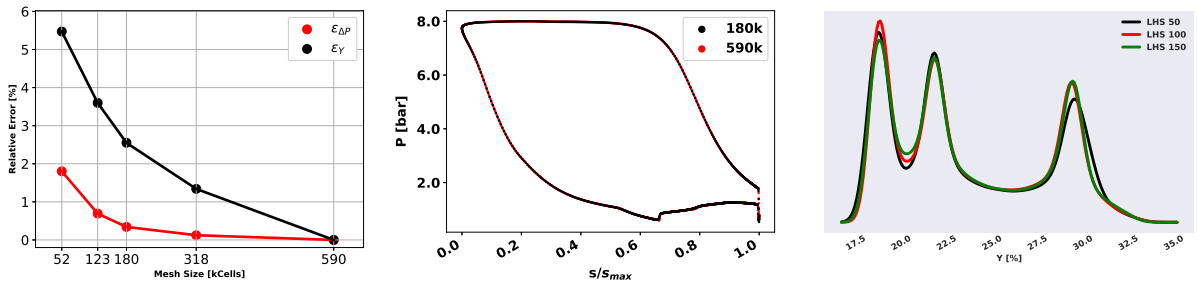

(a) (b) (c)

Figure 5: RANS Grid Analysis on the baseline configuration. (a) ΔP and Y Relative Error, (b) Pressure Distribution comparison between 180k and 590k cells meshes, (c) Y PDF obtained on the 180k cells mesh, for different LHS size.

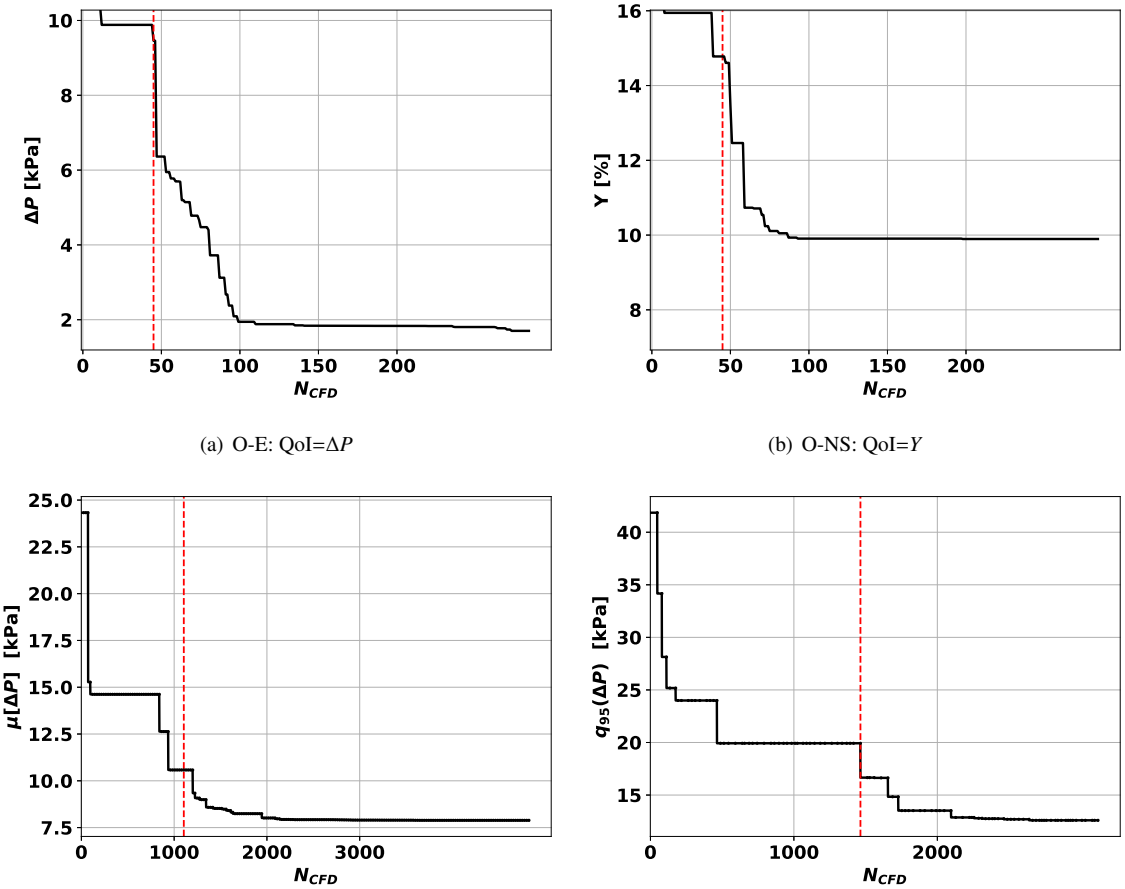

(a) O-E: QoI=ΔP

(b) O-NS: QoI=Y

(c) RO-E-μ: QoI=$\mathbb{E}(\Delta P)$

(d) RO-E-q_{95}: QoI=$q_{95}(\Delta P)$

Figure 6: Convergence curves during the optimization. Best QoI as a function of the number of CFD evaluations. The red vertical line indicates the optimization process start and corresponds to the number of CFD evaluations required for the LHS initial configurations.

Euler-based deterministic optimization. During the optimization, the best profile is obtained after 279 CFD evaluations, with ΔP = 1.70kPa (285 designs are considered in total). Simulations are run in parallel using 8 processors,

except when evaluating the initial DOE where each processor is devoted to in one CFD simulation, in parallel though. The convergence curve shown in Figure 6 (a) indicates a sharp reduction of QoI at the end of the DOE, thus suggesting that the initialization provides a very good approximation of response surface. Then, most of the minimization takes place in the first 50 CFD runs after the DOE. The mass flow rate constraint for the optimal profile (O-E) is satisfied at nominal conditions (See Table 5).

RANS-based deterministic optimization. During the optimization, the best profile is obtained after 198 CFD evaluations, with $Y = 9.9$ % (285 designs are considered in total). Also for the RANS optimization, the convergence curve shown in Figure 6 (b) suggests a proper initialization and a quick convergence, as most of the minimization is achieved in less then 100 CFD runs. The mass flow rate constraint for the optimal profile (O-NS) is not satisfied at nominal conditions ($\dot{m} = 103.9\%\dot{m}_b$), when using the RANS model (Table 5). This might be due to the 'weak' formulation of the constraint, which makes use of the predictive standard deviation based on the Kriging surrogate 3.

Robust Optimization with Mean-based Formulation. An initial DOE of 45 designs is considered (which require 1080 CFD evaluations, since a stochastic evaluation has to be performed for each profile). The best profile is obtained after 157 designs (requiring 3068 CFD evaluations), with $\mu^{\xi}(\Delta P) = 7.9$ kPa (201 blade configurations are considered in total, whose stochastic evaluations require 4824 CFD simulations). The convergence curve Figure 6 (d) shows that a few high-performance designs are found already in the DOE phase, and the identification of the optimum in the following convergence process is relatively fast.

Robust Optimization with Quantile-based Formulation. The Robust Optimization is initialized with a DOE of 45 designs (which in the stochastic framework requires 1416 CFD evaluations). The best profile is obtained after 83 designs (2640 CFD evaluations), with $q_{95}^{\xi}(\Delta P) = 12.6$ kPa. 103 designs are considered (3120 CFD evaluations). The convergence curve in Figure 6 (c) shows again that the DOE is effective in finding few individuals with relatively low q_{95}, followed by a fast process. It is to be noted that the minimization based on the quantile is less demanding than that based on the mean, as almost the half of the blade configurations are required to find the optimum.

To summarize, we have reported the computational cost for each optimization in Appendix A.

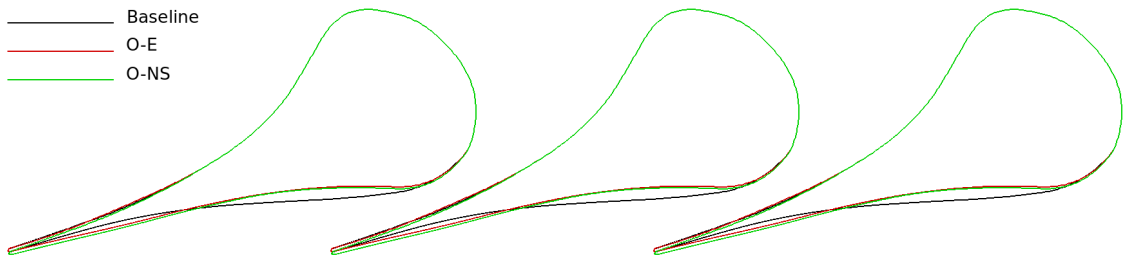

(a) Deterministic

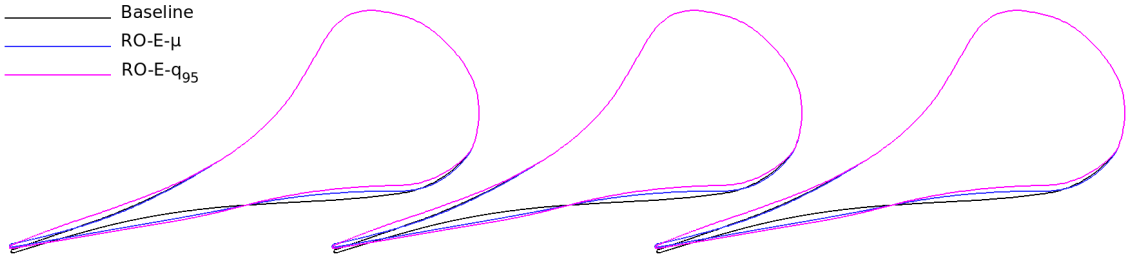

(b) Robust

Figure 7: Blade profiles comparison; top: baseline compared to deterministic optimal blades; bottom: baseline compared to robust optimal blades.

5.3. Optimal blade profiles

The optimal blade profiles obtained with the four optimization processes discussed above are shown in Figure 7 in comparison to the baseline configuration, with frame 7(a) reporting the two deterministic designs and 7(b) the two robust designs.

The two deterministic optimal blades are very similar each other and much different with respect to the baseline layout, especially on the suction side of the blade downstream of the (sonic) throat. The present optimal blades resemble the ones documented in previous design exercises performed on this cascade (e.g., [5],[9],[6]). The deterministic optimization drives the design towards blades featuring an accentuated curvature in the diverging section of the bladed channel, i.e. between the sonic throat and the cascade opening, and an almost straight profile in the region of unguided turning. As it will be discussed in the later section on aerodynamic analysis, such shape allows eliminating the strong shock originated in the baseline cascade flow, with beneficial effects on both the uniformity of the pressure field downstream of the cascade and the cascade loss. This also explains why the two optimizations lead to very similar optimal blades; as a further consideration, the similarity between results obtained with Euler and RANS optimizations indicates that, in the present case, the inviscid model is able to capture the main flow features and hence it is a suitable choice for the more advanced, and more computationally-intensive, robust optimizations.

The two robust designs differ significantly from both the baseline and the deterministic ones. The general action of the optimization is similar to the one commented above, with both the robust-optimal blades featuring a larger curvature on the suction side downstream of the throat and a straight rear suction side. Nonetheless, the area ratio between the cross-sections at the throat and at the opening is lower than that of the deterministic-optimal blades. This can be explained considering that almost all the realizations in the uncertain scenario feature a lower pressure ratio with respect to the nominal one. Since the cross-section at the (sonic) throat is nearly fixed by the constraint on the mass flow rate, the reduction of area-ratio implies a lower area of the cross-section at the blade opening for both the robust-optimal blades with respect to the deterministic-optimal ones. The two blades also feature minor but visible differences, mostly concentrated in the shape of the divergent part of the bladed channel, which also lead to a slight difference in the area-ratio across the divergent, which is higher for the quantile-based optimal blade than for the mean-based one. Instead, the two blade profiles nearly overlap in the rear suction side downstream of the cascade opening and in the trailing edge region, where indeed the flow effects most affecting the QoI (ΔP) take place.

5.4. Analysis of the statistics

A UQ analysis is conducted on the four optimal profiles obtained to assess their performances with the RANS high fidelity model with a 180k cells mesh. As mentioned in Subsection 5.1, $N_{LHS} = 100$ samples are used. A similar analysis is conducted with the inviscid model with 36k cells mesh, used in the optimization process.
The UQ analysis statistics results are summarized in Table 5, obtained using the scalar UQ analysis tools presented in 4.2.1, and commented below.

Nominal Conditions. At nominal conditions, the profiles *O-NS* and *O-E* clearly outperform the other ones with the lowest total pressure loss Y and ΔP. This values of minimal loss and pressure variation are consistent with those obtained in previous deterministic optimization performed on the very same profile [5], [9], and [6]. Moreover, the two deterministic-optimal blades feature very similar losses and identical pressure variability downstream of the cascade, as a further proof of the reliability of inviscid model for the present configuration. Note that also the robust profiles, *RO-E-*μ and *RO-E-*q_{95}, perform similarly at nominal conditions and slightly better than the baseline one with a total pressure loss Y of 15.5%. Even though a probabilistic mass flow constraint is prescribed in the Robust Optimization problems, both *robust* profiles satisfy the deterministic mass flow constraint.

Uncertain Conditions. Mean, standard deviation and 95% quantile of the QoIs ΔP, Y, and the mass flow rate $\dot{m}$ are evaluated for each blade profile using consecutively inviscid and RANS models (Table 5). For each profile, the random mass flow rate shows a rather similar behavior, with a mean value very close to the nominal one and a standard deviation close to 3% of $\dot{m}_b$. It is interesting to note that the performance of the baseline and of the deterministic-optimal profiles deteriorate significantly at off-design conditions. In particular, the *O-E* exhibits $\mathbb{E}[\Delta P] = 16.5\%$ with a large variability associated, quantified by a standard deviation of 10.1% (even larger than that of the baseline

Performances		Profiles				
		Baseline	O-E	O-NS	RO-E-μ	RO-E-q_{95}
Nominal (Euler)	ΔP [kPa]	17.1	1.7	-	12.7	12.2
	Y [%]	16.0	5.4	-	12.1	12.1
	$\dot{m}$ [%]	100.8	100.5	-	101.7	98.3
Nominal (RANS)	ΔP [kPa]	17.5	2.3	2.3	13.6	13.1
	Y [%]	19.0	9.4	9.1	15.5	15.5
	$\dot{m}$ [%]	100.4	100.6	103.9	101.6	98.2
μ, σ, q_{95} (Euler)	ΔP [kPa]	25.7, 6.7, 35.2	16.5, 10.1, 30.4	-	7.9, 3.9, 13.4	8.2, 3.0, 12.7
	Y [%]	20.7, 4.4, 27.8	13.9, 7.1, 26.7	-	8.6, 2.0, 12.8	10.3, 2.2, 14.6
	$\dot{m}$ [%]	100.9, 3.2, 105.9	100.3, 3.2, 105.2	-	101.2, 3.2, 106.3	98.0, 3.1, 102.8
μ, σ, q_{95} (RANS)	ΔP [kPa]	25.4, 6.4, 34.4	16.6, 10.0, 29.5	16.7, 9.9, 29.7	8.2, 3.9, 14.1	8.4, 3.1, 13.2
	Y [%]	23.5, 4.2, 30.0	17.7, 6.8, 29.5	17.6, 7.0, 29.8	12.4, 1.8, 16.1	13.8, 2.1, 18.0
	$\dot{m}$ [%]	100.5, 3.2, 105.4	100.5, 3.2, 105.5	103.9, 3.2, 109.0	101.3, 3.2, 106.3	98.0, 3.1, 102.8

Table 5: Scalar Statistics Analysis for the optimized and baseline profiles. Euler (resp. RANS) quantities are based on CFD evaluations on 36k (resp. 180k) cells meshes. Random scalars are evaluated using $N_{LHS} = 100$ CFD evaluations. $\dot{m}$ is expressed in percentage of $\dot{m}_b = 15.23$ kg/s/m.

one), against an optimal $\Delta P = 2.3kPa$ in nominal conditions; similarly, for the *O-NS* the UQ analysis reveals that $\mathbb{E}[Y] = 17.6\%$ with standard deviation 9.9%, to be compared to $Y = 9.1\%$ at nominal conditions. It is, however, to be noted that the deterministic profiles have been designed for a nominal point which is far from the mean of uncertain conditions (Table 2). This represent a typical scenario of ORC power systems, in which the design (nominal) condition does not correspond to the average of the expected variability; hence, for this technology a robust design approach is particularly beneficial for reducing the sensitivity of the design from the expected variability.

The potential advantages of robust design can be fully appreciated by considering the statistics of the RO-E-μ and RO-E-q_{95} profiles. Considering the inviscid UQ analysis and focusing on ΔP as QoI (for consistency with the model used throughout the optimization), the RO-E-μ profile has the lowest mean value 7.9 kPa and a standard deviation of 3.9%, comparably lower w.r.t. both the deterministic designs. The low variability of the 'conventional' robust optimization is further improved by the here-proposed novel quantile-based design, as the RO-E-q_{95} profile feature both the lowest 95-quantile and the lowest standard deviation of 3.0%, with only a slight increase of mean value (8.2 kPa) w.r.t. the mean-based design. The lowest variability of the RO-E-q_{95} blade is confirmed by the high-fidelity RANS analysis, which provides nearly identical results of the inviscid one in terms of ΔP; this, once again, indicates that the inviscid model is able to provide a reliable design when combined with a proper selection of QoI.

Focusing now on the blade performance in terms of loss coefficient, and considering the RANS UQ analysis, the two robust-optimal blades behave almost equivalently, the RO-E-μ blade slightly outperforming the RO-E-q_{95} one both in terms of both mean value and variability. This is not in contradiction with the optimization, which used another QoI as fitness function. The results of the present robust optimization indicates that a quantile-based approach has the potential to minimize the variability of loss coefficient, if set with Y as QoI and using the RANS model, at the expense of a significant increase of computational cost Note that the 36k Euler simulation takes 500s; the 52k RANS simulation takes 1200s, on 8 procs. Roughly, the CPU time is then multiplied by 16. In light of the present results, the similar performance of the two robust-optimal blades might not justify such increased effort.

The complete picture of the stochastic properties of the baseline and optimal blades is provided by the plots of the PDF for ΔP, Y and $\dot{m}$, reported in Figures 8, 9, and 10 respectively. In these figures, the PDFs computed with Euler and RANS models are reported in separate frames, the former considering only the baseline and the optimal blades obtained with inviscid optimization process (i.e., *O-E*, RO-E-μ, and RO-E-q_{95}) and the latter featuring also the *O-NS* one. First considering ΔP as QoI, it is evident that the baseline blade has a relatively large variability (which, in such PDF plots, can be visualized as the PDF 'support' which is, in turn, quantified as the difference between the 5% and the 95% quantiles). This illustration of the difference between 5% and 95% quantiles provides a good representation of the PDF support. The deterministic-optimal blades, which feature a very similar PDF when evaluated with a high-fidelity RANS model, perform generally better than the baseline one but exhibit a very large variability, so that their support overlaps the one of the baseline in a large region ($16kPa \leq \Delta P \leq 32kPa$); this means that in a very significant

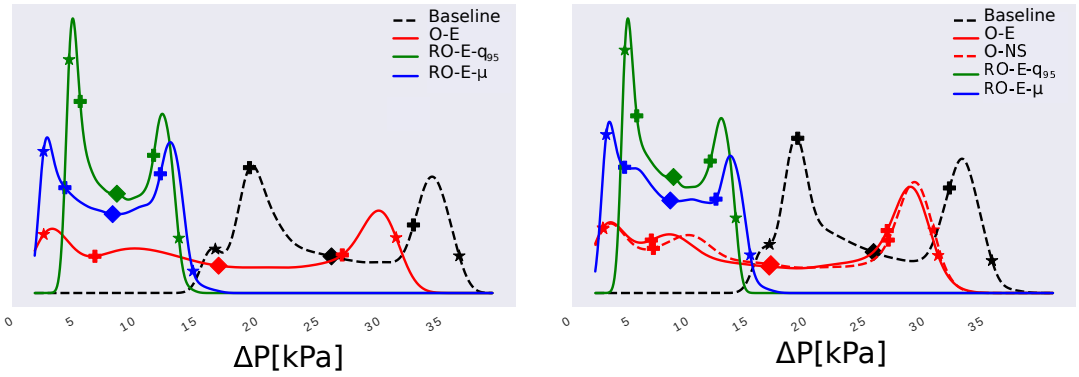

(a) ΔP: Euler 36kcell mesh

(b) ΔP: RANS 180kcell mesh

Figure 8: PDF comparison between the optimized and baseline profiles. "Plus" dots indicate $\mu \pm \sigma$, square dots indicate μ, star dots indicate respectively 5% and 95% quantiles. $N_{LHS} = 100$ samples considered.

fraction of the possible realizations of the process, the baseline can actually outperform the deterministic-optimal blades. From this perspective, the robust-optimal blades provide a crucial improvement with respect to deterministic-optimal ones; not only the mean value of QoI is much lower than that of the other blades, but the entire support of their PDFs is significantly reduced and, especially, it is almost completely decoupled from that of the baseline blade; this ensures that the robust-optimal blades outperform the baseline configuration in almost all the possible realizations of the process within the variability range. When comparing the PDFs of the robust-optimal blades, some differences emerge in a context of global similarity; in particular, the quantile-based approach guarantees not only to minimize the 95% quantile, but in general to slightly reduce the support of the PDF, and so the variability as already seen in terms of the standard deviation. From this perspective, the novel quantile-based approach is competitive w.r.t. the more standard mean-based approach both in terms of computational cost (as already commented) and in terms of the stochastic performance of the optimization outcome.

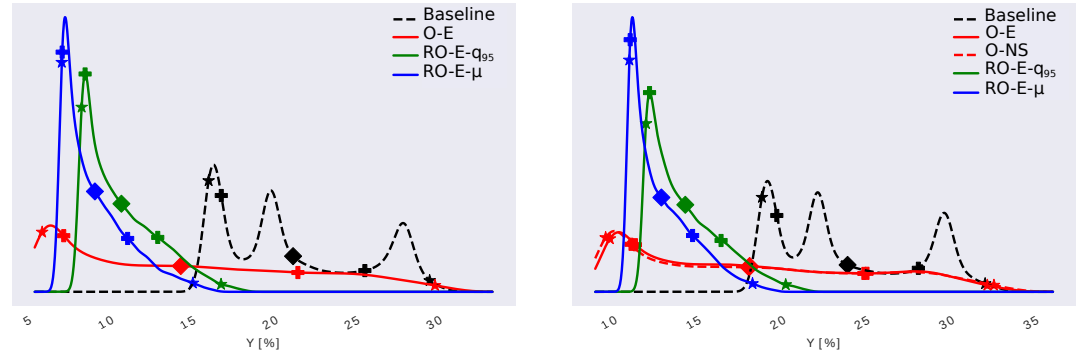

(a) Y: Euler 36kcell mesh

(b) Y: RANS 180kcell mesh

Figure 9: PDF comparison between the optimized and baseline profiles. "Plus" dots indicate $\mu \pm \sigma$, square dots indicate μ, star dots indicate respectively 5% and 95% quantiles. $N_{LHS} = 100$ samples considered.

The considerations reported above also hold for the PDFs of Y. The two deterministic-optimal blades are still equivalent and with a large support which overlaps largely with the one of the baseline; again, the robust-optimal

blades provide a much smaller support w.r.t. the baseline one, with an almost complete decoupling. As already noted when commenting the statistics, the two robust-optimal blades feature similar stochastic properties, with the RO-E-μ blade providing a slightly smaller mean value and 95% quantile; however, the two supports are almost entirely overlapped, demonstrating that the two robust-optimal blades are practically equivalent in terms of loss coefficient.

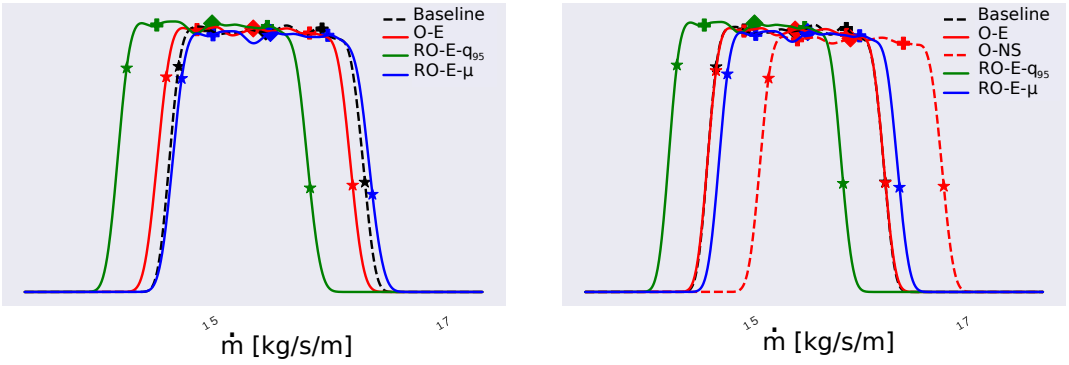

(a) $\dot{m}$: Euler 36kcell mesh

(b) $\dot{m}$: RANS 180kcell mesh

Figure 10: PDF comparison between the optimized and baseline profiles. "Plus" dots indicate $\mu \pm \sigma$, square dots indicate μ, star dots indicate respectively 5% and 95% quantiles. $N_{LHS} = 100$ samples considered.

Finally considering the flow rate, all the PDFs are qualitatively similar and exhibit a nearly identical support. As for the entire range of variability considered the cascades is always in choked-flow conditions, the shape and the support of the PDFs directly depend of the variability in the inlet total conditions and the PDF takes a trapezoidal shape, as discussed in detail in [48]. Some of the PDFs are slightly shifted, with the RO-E-q_{95} blade featuring a slightly smaller mean and quantiles and the *O-NS* blade exhibiting a slightly higher mean and quantiles, but most of the realizations of all the optimal blades are within the acceptability range of probabilistic constraint. Note that for all blades, all the realizations are not within the acceptability range of the probabilistic constraint, since, finally, only the mean is constrained to be within that range.

5.5. Physical Analysis

This subsection discusses the aerodynamics of the baseline and optimal blades under uncertain flow conditions, considering high-fidelity RANS simulations, with the aim of explaining the properties of the optimal blades on the basis of physical considerations.

Three classes of quantities are considered. The Mach number contour fields at nominal conditions are first shown in Figure 11. Then, the UQ framework for vector statistics presented in Subsubsection 4.2.3 and the CFD evaluations performed in Subsubsection 5.4 are used to evaluate statistics of flow fields; in particular, the contours of mean and CoV of the Mach number are considered and are reported in Figures 12 and 13 respectively. 73 modes out of 100 PCA modes are retained in the analysis, corresponding to a cumulative energy conservation beyond 99.99%.

The figures of this subsection show the contours for the baseline and for all the optimal blades, and are supplemented by corresponding isentropic Mach number distributions over the blade surface. The isentropic Mach number is evaluated assuming an isentropic expansion from total upstream condition to the local static pressure on the blades, and is commonly used in turbomachinery application to highlight relevant cascade features such as shocks, overspeeds, and adverse pressure gradients.

Nominal Mach contours. At nominal conditions, the baseline blade exhibits the onset of a strong shock resulting from the coalescence of train of compression waves generated on the curved rear suction side.

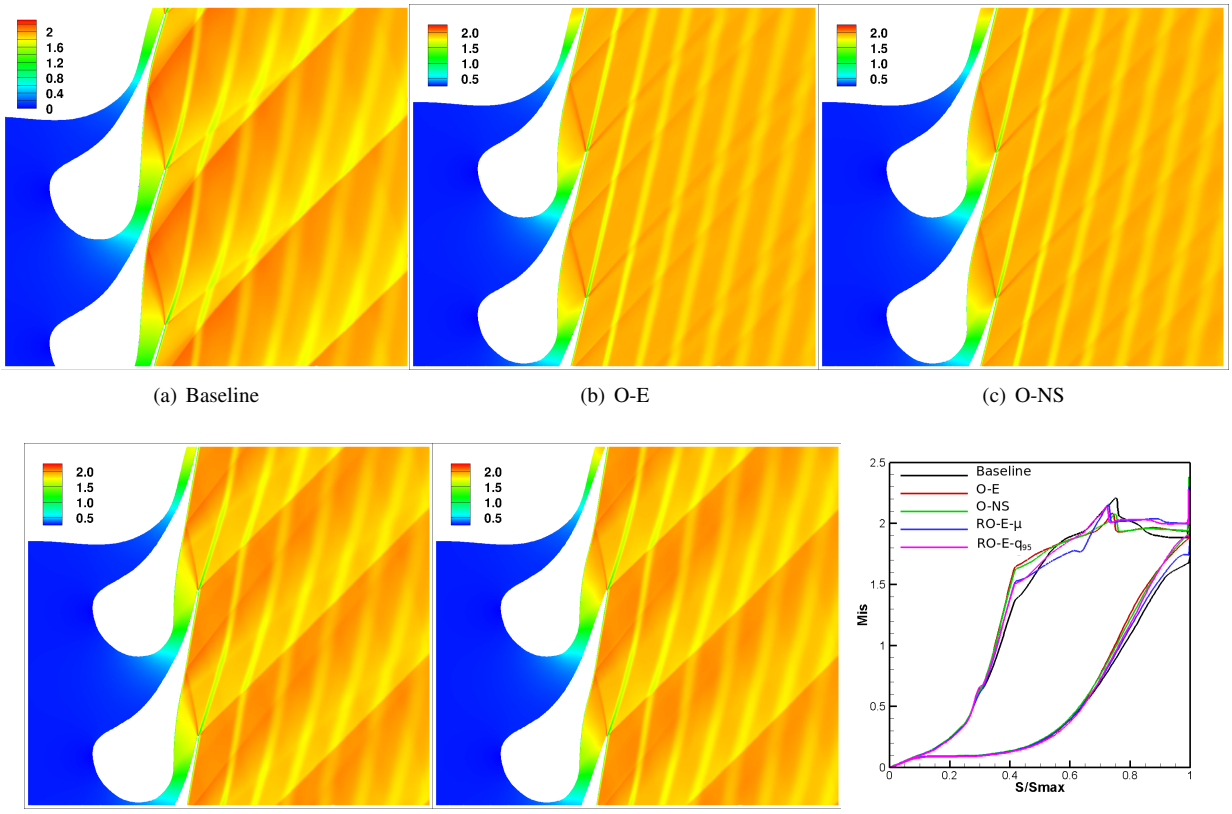

(a) Baseline (b) O-E (c) O-NS

(d) RO-E-μ (e) RO-E-q_{95} (f) M_{is} profile

Figure 11: Mach contours at Nominal conditions. [RANS, 180k cells mesh]

The strong shock is responsible for both the high loss and the large pressure gradients affecting the cascade-exit flow field. When the blade is optimized for the nominal condition only, the optimization removes the main shock by identifying optimal blades with straight shape in the rear part; since the trailing edge of the blade is geometrically constrained, the optimization cannot eliminate the fish-tail shock system generated at the trailing edge.

Considering the M_{is} profiles, the comparison between the deterministic-optimal blades and the baseline one clearly shows that the latter features a higher over-speed, followed by a shock (which is the reflection on the blade surface of one trailing edge shock generated on the adjacent blade) and by a diffusion which ultimately leads to the generation of the main shock; while the reflected shock is present also in the optimal blades, and depends on the constraint in the trailing edge thickness, the subsequent diffusion is absent from the pressure distribution of the deterministic-optimal blades. The two deterministic-optimal blades are shown, once again, to perform equivalently even though obtained with different flow models.

The flow uniformity provided by the deterministic optimization is not achieved with the robust-optimal blades, which instead exhibit the onset of a strong shock in the cascade-exit flow field. However, the origin of this shock is completely different from that of the baseline shock.

As a matter fact, the shock is generated on the suction side of the trailing edge and not as a result of a diffusion on the blade. This is further confirmed by the M_{is} profiles, which show no diffusion on the suction side downstream of the reflected shock for both the robust-optimal profiles. The shock is simply originated by the fact that the robust-optimal blade are designed for having good performance in a range of conditions which feature, in average, lower expansion ratio than in the nominal condition. As already commented when discussing the blade shape, the robust-optimal blades have a lower area-ratio across the divergent w.r.t. the deterministic-optimal ones. As a result, when operated in nominal condition, the robust-optimal blades are in fact in post-expansion, which as well known leads to the onset of

a shock at the trailing edge.

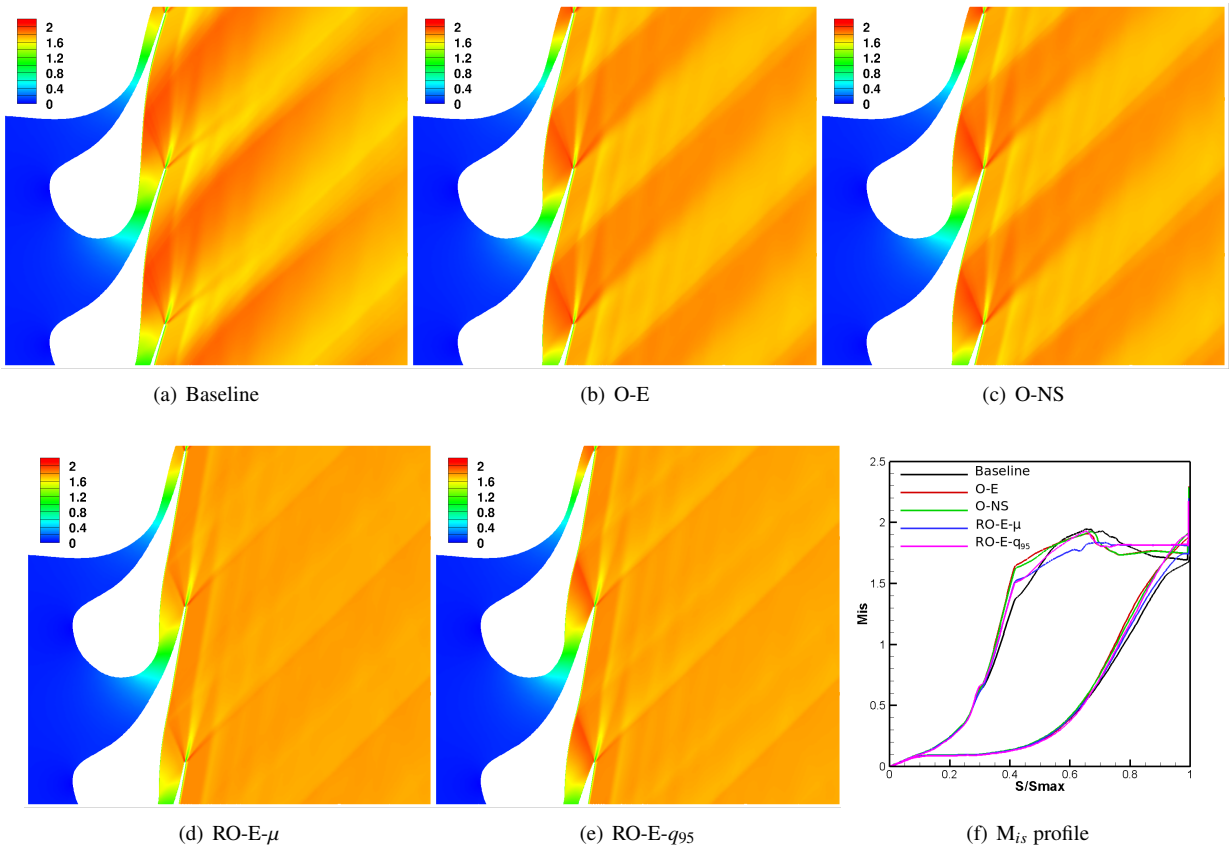

(a) Baseline (b) O-E (c) O-NS

(d) RO-E-μ (e) RO-E-q_{95} (f) M_{is} profile

Figure 12: Mach contours mean considering uncertain operating conditions, evaluated by means of PCA UQ (Subsubsection 4.2.3) [RANS, 180k cells mesh, $N_{LHS} = 100$]

Mean Mach contours. In light of the flow features emerging in nominal conditions, it is interesting to analyze the mean aerodynamics of the optimal blades. It is worth noticing, at first, that commenting a mean contour is not straightforward, as each point in the mesh is result of a statistical procedure and, hence, the field is not reproducing the flow in a specific condition; therefore, only the general trends can be commented while the analysis of detailed features might be misleading. The distribution computed for the baseline blade shows a similar character of that commented for the nominal condition, even though with smeared gradients. This indicates that the baseline blade suffers from the effects of the rear-shock in whole variability range; this is reasonable since the flow in the rear suction side of the blade remains supersonic for all considered conditions, so the curved shape of the always leads to the onset of the rear shock. As a further confirmation of what above, the mean profile of M_{is} shows a large diffusion region downstream of the mean over-speed.

The deterministic-optimal blades improve the behavior of the baseline one, but the uniformity observed in nominal condition is not visible anymore; conversely, clear variations in mean Mach number appear in the cascade-exit flow field, which seem to be correlated to the shock-pattern generated at the trailing edge. This is motivated by the area-ratio of both the deterministic-optimal blades, which is too large for most of the realizations occurring within the prescribed variability; as a result, the cascade often operates in post-compression condition, which leads to the onset of relatively strong shocks at the trailing edge.

The robust optimization is able to greatly reduce the effects discussed above; in particular, RO-E-μ blade features an almost uniform mean Mach number distribution at the cascade exit, proving that the mean-based optimization is able to select the most suitable blade configuration over the range of variability. Interestingly, the RO-E-q_{95} blade

provides a similar flow uniformity at the cascade exit, even though the quantile-based optimization does not consider explicitly the mean values in the optimization algorithm. Differences between the two robust-optimal cascade exist and are concentrated in the divergent, with the RO-E-q_{95} blade featuring a higher over-speed; however, in the rear suction side downstream of the reflected shock the M_{is} profiles of the two blades become nearly identical, thus leading to a very similar cascade-exit mean flow field.

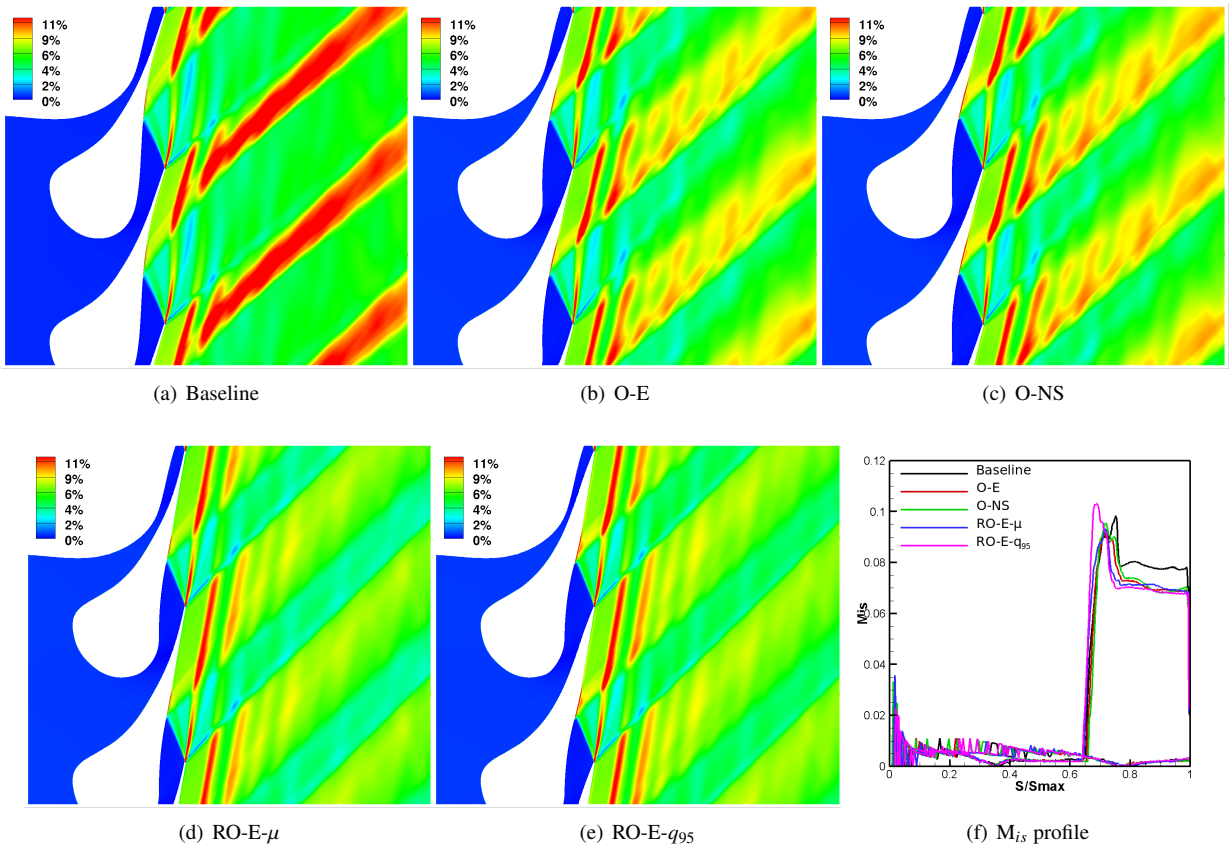

(a) Baseline (b) O-E (c) O-NS

(d) RO-E-μ (e) RO-E-q_{95} (f) M_{is} profile

Figure 13: Mach contours CoV [%] considering uncertain operating conditions, evaluated by means of PCA UQ (Subsubsection 4.2.3) [RANS, 180k cells mesh, $N_{LHS} = 100$]

CoV Mach contours. In order to highlight the local distribution of variability over the flow field, the CoV coefficient (defined as the ratio between the standard deviation and the mean) is now analyzed. First considering the baseline blade, very high CoV is established in the region interested by the compression wave / shock, suggesting that the main shock featuring this blade undergoes a significant evolution across the considered range of variability. A somehow similar patter is found for the deterministic-optimal blades with a generally high CoV in the region comprised between the reflected shock and the trailing edge shock. A net reduction of CoV is found when analyzing the robust-optimal blades, which anyway exhibit a CoV distribution similar to that of the other blades. This result suggests that, when a proper QoI is selected, the application of the robust design allows reducing the variability in the entire flow field.

6. Conclusion

A Robust optimization method based on a quantile formulation is fully documented and applied to the design of supersonic ORC cascade operating in the non-ideal regime. We provide evidence about the advantages of a quantile-based formulation with respect to a conventional mean-based robust optimization. By applying the novel quantile-based procedure, we obtain a RO-E-q_{95} profile, which has the lowest 95-quantile and the smallest standard deviation

of 3.0%, with only a slight increase of mean value (8.2 kPa) w.r.t. the mean-based design. In the case of interest here, a significant control about the variability of the PDF through the quantile formulation is obtained with a lower computational cost with respect to the mean. More generally, it seems that even in a case when the computational cost could be of the same order of magnitude, the choice of a quantile formulation should be preferred.

The blades obtained by both the quantile-based and mean-based robust optimizations outperform significantly (in stochastic sense) the ones achieved by resorting to conventional deterministic optimizations, which actually provide good performance only in a very narrow range of operation close to the design nominal condition.

Concerning the optimal blades, the flow uniformity provided by the deterministic optimization is not achieved with the robust-optimal blades, which exhibit the onset of a sharp shock in the cascade-exit flow field. This shock comes from the fact that the robust-optimal blades are designed for having good performance in a range of conditions which have a lower expansion ratio than in the nominal state. When operated in nominal condition, the robust-optimal blades are in fact in post-expansion, which as well known leads to the onset of a shock at the trailing edge. The two robust designs differ significantly with respect to the deterministic ones, as the area ratio between the cross-sections at the throat and the opening is lower than that of the deterministic-optimal blades. This behavior can be explained considering that almost all the realizations in the uncertain scenario feature a lower pressure ratio with respect to the nominal one. The two blades also feature minor but visible differences mostly concentrated in the shape of the divergent part of the bladed channel, which also leads to a slight difference in the area-ratio across the divergent.

Another relevant point observed is that the robust optimization with low-fidelity solver can yield a design with better performances (on both Euler and RANS evaluations) than the one coming from a purely deterministic optimization using a high-fidelity RANS solver. This behavior has a great interest in ORC turbine optimization since it could provide a concrete alternative approach with respect to the current procedures to guarantee better the robustness of the design at a moderate computational cost.

Globally, in this paper, high-fidelity RANS analysis provides nearly identical results of the inviscid one in terms of ΔP. This behavior shows that the inviscid model can provide a reliable design when combined with a proper selection of QoI.

Future work will be devoted to the use of numerical strategies enabling an adaptive computation of the quantile during the optimization. In particular, we aim to use the SaBBA framework developed in [49, 50], coupled eventually to a multi-fidelity approach.

Appendix A. Computational Cost

In the present section, details about the CPU cost during the optimization process are discussed . All computations are done on a standard laptop with an i7-6820HQ CPU at 2.70GHz equipped with 8 processors. Detailed information is available in Table A.6. In the four optimization cases, $N^{\mathbf{x}}_{LHS} = 45$ profiles are considered for the initial DOE, that can be considered independently. Then, the EI loop sequentially provides a new profile to be analysed.

Deterministic Optimization: Euler. The initial DOE is evaluated in parallel. $N_{iter} = 246$ iterations are totally required. The best profile is obtained after 279 CFD simulations.

Deterministic Optimization: NS . $N_{iter} = 285$ iterations are totally required. During the optimization loop, each RANS simulation is run with 8 processors. The best profile is optained after 198 simulations.

Quantile-Based Optimization. The initial DOE step requires 1808 CFD calls. For a given profile, ~ 32 CFD calls corresponding to ~ 4 iterations are necessary to evaluate the so-called 95% quantile. In total, $N_{profiles} = 103$ profiles are considered requiring 3120 CFD calls, in $N_{iter} = 390$ iterations. The 83^{th} profile is the best, requiring 2640 CFD calls.

Mean-Based Optimization. The quantile-based optimization initial DOE is used in order to compare the two robust strategies from the same initial designs. For any given profile, 24 CFD calls corresponding to 3 iterations are necessary to evaluate the mean, leading to a total number of $N_{iter} = 603$ iterations. The 157^{th} profile is the best, requiring 3768 CFD calls.

Note that this cost is about $\sim 50\%$ more than for the quantile-based optimization). For the present case, 16 CFD runs in the stochastic space for evaluating the mean is very conservative, but necessary for the proposed algorithm. As a general comment, a relevant point to raise is the interest in optimizing a quantile since a higher control of the PDF variability is possible with a comparable cost of computing a quantile with respect to the mean.

	O-E	O-NS	RO-E-q_{95}	RO-E-μ
Initial DOE	45(45)	45(45)	45(1416)	45(1080)
$N_{profiles}(N_{CFD})$	285(285)	285(285)	103(3120)	201(4824)
N_{iter} (8 PROC)	246	285	390	603
Time/iteration	500s	1200s (8 procs)	500s	500s

Table A.6: CPU cost required during the optimization process for the three profiles in terms of time and number of CFD calls. $N_{profiles}$ is the number of profiles considered during optimization, N_{CFD} the number of CFD evaluations required to assess the corresponding profiles and N_{iter} the number of iterations necessary assuming parallel computations with 8 processors.

References

[1] Macchi, E.. Theoretical basis of the Organic Rankine Cycle. Woodhead Publishing. ISBN 978-0-08-100510-1; 2017, p. 3–24.

[2] Colonna, P., Casati, E., Trapp, C., Mathijssen, T., Larjola, J., Turunen-Saaresti, T., et al. Organic Rankine Cycle Power Systems: From the Concept to Current Technology, Applications, and an Outlook to the Future. Journal and Engineering for Gas Turbines and Power 2015;137(100801).

[3] Pironneau, O.. On optimum design in fluid mechanics. Journal of Fluid Mechanics 1974;64(1):97–110. doi:10.1017/S0022112074002023.

[4] Spinelli, A., Cammi, G., Gallarini, S., Zocca, M., Cozzi, F., Gaetani, P., et al. Experimental evidence of non-ideal compressible effects in expanding flow of a high molecular complexity vapor. Experiments in Fluids 2018;59(8).

[5] Pini, M., Persico, G., Pasquale, D., Rebay, S.. Adjoint method for shape optimization in real-gas flow applications. ASME Journal of Engineering for Gas Turbines and Power 2015;137(3).

[6] Vitale, S., Albring, T.A., Pini, M., Gauger, N.R., Colonna, P., et al. Fully turbulent discrete adjoint solver for non-ideal compressible flow applications. Journal of the Global Power and Propulsion Society 2017;1:Z1FVOI.

[7] Rubino, A., Pini, M., Colonna, P., Albring, T., Nimmagadda, S., Economon, T., et al. Adjoint-based fluid dynamic design optimization in quasi-periodic unsteady flow problems using a harmonic balance method. Journal of Computational Physics 2018;.

[8] Pasquale, D., Ghidoni, A., S., R.. Shape optimization of an Organic Rankine Cycle radial turbine nozzle. Journal and Engineering for Gas Turbines and Power 2013;135(042308).

[9] Persico, G., Rodriguez-Fernandez, P., Romei, A.. High-fidelity shape optimization of non-conventional turbomachinery by surrogate evolutionary strategies. Journal of Turbomachinery 2019;141(8):081010–081010–11.

[10] Persico, G.. Evolutionary Optimization of Centrifugal Nozzles for Organic Vapours. Journal of Physics: Conference Series 2017;821(012015).

[11] Persico, G., Pini, M.. Fluid dynamic design of Organic Rankine Cycle turbines. Woodhead Publishing. ISBN 978-0-08-100510-1; 2017, p. 253–297.

[12] Pini, M., Persico, G., Dossena, V.. Robust adjoint-based shape optimization of supersonic turbomachinery cascades. In: ASME Turbo Expo 2014: Turbine Technical Conference and Exposition. American Society of Mechanical Engineers; 2014, p. V02BT39A043–V02BT39A043.

[13] Amir, O., Sigmund, O., Lazarov, B.S., Schevenels, M.. Efficient reanalysis techniques for robust topology optimization. Computer Methods in Applied Mechanics and Engineering 2012;245-246:217 – 231. URL: http://www.sciencedirect.com/science/article/pii/S0045782512002289. doi:https://doi.org/10.1016/j.cma.2012.07.008.

[14] Keshavarzzadeh, V., Fernandez, F., Tortorelli, D.A.. Topology optimization under uncertainty via non-intrusive polynomial chaos expansion. Computer Methods in Applied Mechanics and Engineering 2017;318:120 – 147. URL: http://www.sciencedirect.com/science/article/pii/S0045782516313019. doi:https://doi.org/10.1016/j.cma.2017.01.019.

[15] Zhang, J., Taflanidis, A., Medina, J.. Sequential approximate optimization for design under uncertainty problems utilizing kriging metamodeling in augmented input space. Computer Methods in Applied Mechanics and Engineering 2017;315:369 – 395. URL: http://www.sciencedirect.com/science/article/pii/S0045782516314529. doi:https://doi.org/10.1016/j.cma.2016.10.042.

[16] Jin, R., Du, X., Chen, W.. The use of metamodeling techniques for optimization under uncertainty. Structural and Multidisciplinary Optimization 2003;25(2):99–116. URL: https://doi.org/10.1007/s00158-002-0277-0. doi:10.1007/s00158-002-0277-0.

[17] LEE, K.H., PARK, G.J.. A global robust optimization using kriging based approximation model. JSME International Journal Series C Mechanical Systems, Machine Elements and Manufacturing 2006;49(3):779–788. doi:10.1299/jsmec.49.779.

[18] Janusevskis, J., Le Riche, R.. Simultaneous kriging-based estimation and optimization of mean response. Journal of Global Optimization 2013;55(2):313–336. URL: https://doi.org/10.1007/s10898-011-9836-5. doi:10.1007/s10898-011-9836-5.

[19] Huang, D., Allen, T.T., Notz, W.I., Zeng, N.. Global Optimization of Stochastic Black-Box Systems via Sequential Kriging Meta-Models. Journal of Global Optimization 2006;34(3):441–466. URL: https://doi.org/10.1007/s10898-005-2454-3. doi:10.1007/s10898-005-2454-3.

[20] Picheny, V., Ginsbourger, D., Richet, Y.. Noisy Expected Improvement and on-line computation time allocation for the optimization of simulators with tunable fidelity; 2010. URL: https://hal.archives-ouvertes.fr/hal-00489321; working paper or preprint.

[21] Congedo, P., Geraci, G., Abgrall, R., Pediroda, V., Parussini, L.. Tsi metamodels-based multi-objective robust optimization. Engineering Computations (Swansea, Wales) 2013;30(8):1032–1053.
[22] Bufi, E.A., Camporeale, S.M., Cinnella, P.. Robust optimization of an organic rankine cycle for heavy duty engine waste heat recovery. Energy Procedia 2017;129:66 – 73. URL: http://www.sciencedirect.com/science/article/pii/S1876610217341048. doi:https://doi.org/10.1016/j.egypro.2017.09.190; 4th International Seminar on ORC Power SystemsSeptember 13-15th 2017POLITECNICO DI MILANOBOVISA CAMPUSMILANO, ITALY.
[23] Bufi, E.A., Cinnella, P.. Robust optimization of supersonic orc nozzle guide vanes. Journal of Physics: Conference Series 2017;821(1):012014. URL: http://stacks.iop.org/1742-6596/821/i=1/a=012014.
[24] Schöbi, R., Sudret, B., Marelli, S.. Rare event estimation using polynomial-chaos kriging. ASCE-ASME Journal of Risk and Uncertainty in Engineering Systems, Part A: Civil Engineering 2016;3(2):D4016002.
[25] E. Brochu, V.M.C., de Freitas, N.. A tutorial on bayesian optimization of expensive cost functions, with application to active user modeling and hierarchical reinforcement learning. arXiv:10122599 2010;.
[26] Colonna, P., Harinck, J., Rebay, S., Guardone, A.. Real-gas effects in organic rankine cycle turbine nozzles. Journal of Propulsion and Power 2008;24(2):282–294.
[27] Palacios, F., Colonno, M.F., Aranake, A.C., Campos, A., Copeland, S.R., Economon, T.D., et al. Stanford University Unstructured (SU2): An open-source integrated computational environment for multi-physics simulation and design. In: 51st AIAA Aerospace Sciences Meeting and Exhibit. 2013,.
[28] Economon, T.D., Mudigere, D., Bansal, G., Heinecke, A., Palacios, F., Park, J., et al. Performance optimizations for scalable implicit {RANS} calculations with {SU2}. Computers & Fluids 2016;129:146 – 158. URL: http://www.sciencedirect.com/science/article/pii/S0045793016300214. doi:http://dx.doi.org/10.1016/j.compfluid.2016.02.003.
[29] Pini, M., Vitale, S.,, , Colonna, P., Gori, G., Guardone, A., et al. Su2: the open-source software for non-ideal compressible flows. In: NICFD 2016: 1st International Seminar on Non-Ideal Compressible-Fluid Dynamics for Propusion & Power. Varenna, Italy; 2016,.
[30] Gori, G., Zocca, M., Cammi, G., Spinelli, A., Guardone, A.. Experimental assessment of the open-source su2 cfd suite for orc applications. Energy Procedia 2017;129(Supplement C):256 – 263. doi:https://doi.org/10.1016/j.egypro.2017.09.151.
[31] Vitale, S., Gori, G., Pini, M., Guardone, A., Economon, T.D., Palacios, F., et al. Extension of the su2 open source cfd code to the simulation of turbulent flows of fuids modelled with complex thermophysical laws. AIAA Paper 2015;2760:2015.
[32] Roe, P.L.. Approximate riemann solvers, parameter vectors, and difference schemes. J Comput Phys 1981;43(2):357–372. URL: http://linkinghub.elsevier.com/retrieve/pii/0021999181901285.
[33] Vinokur, M., Montagné, J.L.. Generalized flux-vector splitting and roe average for an equilibrium real gas. J Comput Phys 1990;89:276.
[34] Guardone, A., Vigevano, L.. Roe linearization for the van der Waals gas. J Comput Phys 2002;175:50–78.
[35] Menter, F.. Zonal two equation kw turbulence models for aerodynamic flows. In: 23rd fluid dynamics, plasmadynamics, and lasers conference. 1993, p. 2906.
[36] Giles, M.B.. Nonreflecting boundary conditions for euler equation calculations. AIAA journal 1990;28(12):2050–2058.
[37] De Boer, A., Van der Schoot, M., Bijl, H.. Mesh deformation based on radial basis function interpolation. Computers & structures 2007;85(11-14):784–795.
[38] Hoschek, J., Lasser, D., Schumaker, L.L.. Fundamentals of computer aided geometric design. AK Peters, Ltd.; 1993.
[39] Farin, G.. Curves and Surfaces for CAGD: A Practical Guide. 5 ed.; San Francisco, CA, USA: Morgan Kaufmann Publishers Inc.; 2002.
[40] C. E. Rasmussen, C.W.. Gaussian Processes for Machine Learning. the MIT Press; 2006.
[41] GPy, . GPy: A gaussian process framework in python. http://github.com/SheffieldML/GPy; since 2012.
[42] Santner, T., Williams, B., Notz, W.. The design and analysis of computer experiments. New York: Springer; 2013.
[43] Miranda, A.A., Le Borgne, Y.A., Bontempi, G.. New routes from minimal approximation error to principal components. Neural Processing Letters 2008;27(3):197–207.
[44] Nikolaus Hansen, . CMA. https://pypi.python.org/pypi/cma; 2018.
[45] Denos, R., Arts, T., Paniagua, G., Michelassi, V., Martelli, F.. Investigation of the Unsteady Aerodynamics in a Transonic Turbine Stage. ASME J Turbomach 2001;123(1):81–89.
[46] Miller, R., Moss, R., Ainsworth, R., Harvery, N.. Wake, Shock, and Potential Field Interactions in a 1.5 Stage Turbine—Part I: Vane-Rotor and Rotor-Vane Interaction. ASME J Turbomach 2003;125(1):33–39.
[47] Han, Z.H., Abu-Zurayk, M., Görtz, S., Ilic, C.. Surrogate-based aerodynamic shape optimization of a wing-body transport aircraft configuration. In: Symposium on AeroStructures. Springer; 2015, p. 257–282.
[48] Romei, A., Congedo, P.M., Persico, G.. Assessment of deterministic shape optimizations within a stochastic framework for supersonic organic rankine cycle nozzle cascades. Journal of Engineering for Gas Turbines and Power 2019;141(7):071019–071019–11.
[49] Rivier, M., Congedo, P.M.. Surrogate-Assisted Bounding-Box Approach for Optimization Problems with Approximated Objectives. Research Report RR-9155; Inria; 2018. URL: https://hal.inria.fr/hal-01713043.
[50] Rivier, M., Congedo, P.M.. Surrogate-Assisted Bounding-Box Approach Applied to Constrained Multi-Objective Optimisation Under Uncertainty. Research Report RR-9214; Inria Bordeaux Sud-Ouest ; Inria Saclay; 2018. URL: https://hal.inria.fr/hal-01897399.